JANUARY 2024

M.Sc. in Optical Engineering

BETÜL KONAKLI YAZGAN

REPUBLIC OF TURKEY

GAZİANTEP UNIVERSITY

GRADUATE SCHOOL OF NATURAL & APPLIED SCIENCES

SPACEBORNE TELE-OBJECTIVE DESIGN FOR EARTH IMAGING

M.Sc. THESIS

IN

OPTICAL ENGINEERING

BY

BETÜL KONAKLI YAZGAN

JANUARY 2024

SPACEBORNE TELE-OBJECTIVE DESIGN FOR EARTH IMAGING

M.Sc. Thesis

in

Optical Engineering

Gaziantep University

Supervisor

Prof. Dr. Ahmet BİNGÜL

Co-Supervisor

Dr. Özgür KARCI

by

Betül KONAKLI YAZGAN

January 2024

I hereby declare that all information in this document has been obtained and presented in accordance with academic rules and ethical conduct. I also declare that, as required by these rules and conduct, I have fully cited and referenced all material and results that are not original to this work.

Betül KONAKLI YAZGAN

ABSTRACT

SPACEBORNE TELE-OBJECTIVE DESIGN FOR EARTH IMAGING

KONAKLI YAZGAN, Betül
M.Sc. in Optical Engineering
Supervisor: Prof. Dr. Ahmet BİNGÜL
Co-Supervisor: Dr. Özgür KARCI
January 2024
63 pages

This thesis presents an electro-optic camera design to fit into a 6U CubeSat platform for Earth observation from the low Earth orbit (LEO). The design is aimed to achieve a 4.5 m ground sampling distance (GSD) at 400 km altitude. The optical design of the camera is based on a refractive, telephoto objective architecture consisting of six spherical lenses whose optical materials are compatible with the space environment. An F/5.5 telephoto objective, near diffraction-limited performance over 2.6-degree of the full field of view (FFOV) is optimized utilizing a ray-tracing software (i.e., OpticStudio) for panchromatic imaging between the spectrum of 450 – 700 nm. A commercial, complementary metal-oxide semiconductor (CMOS) 2-D imaging sensor is selected to provide a better than 15 km swath width. A tolerance analysis of the optical design has been carried out to identify limitations related to the alignment and optical manufacturing. The modulation transfer function (MTF) and signal-to-noise ratio (SNR) budgeting analysis are also performed to show the performance of the electro-optic camera design.

Key Words: CubeSats, optical design, tolerance analysis, telephoto optical system, electro-optic camera.

ÖZET

DÜNYA GÖRÜNTÜLEMESİ İÇİN UZAY UYUMLU TELE-OBJEKTİF TASARIMI

KONAKLI YAZGAN, Betül
Yüksek Lisans, Optik Mühendisliği Bölümü
Danışman: Prof. Dr. Ahmet BİNGÜL
İkinci Danışman: Dr. Özgür KARCI
Ocak 2024
63 sayfa

Bu tez, alçak Dünya yörüngesinden (LEO) yer gözlemi için 6U Küpsat platformuna sığacak bir elektro-optik kamera tasarımı sunmaktadır. Tasarım, 400 km irtifada 4.5 m yer örnekleme mesafesi (GSD) elde etmeyi amaçlamaktadır. Kameranın optik tasarımı, optik malzemeleri uzay ortamıyla uyumlu olan altı küresel mercekten oluşan kırıcı telefoto objektif mimarisine dayanmaktadır. Tam görüş alanının (FFOV) 2.6 derecesi üzerinde kırınım sınırına yakın performans gösteren bir F/5.5 telefoto objektif, 450-700 nm spektrumu arasında pankromatik görüntüleme için bir ışın izleme yazılımı (OpticStudio) kullanılarak optimize edilmiştir. Ticari, tümleyici metal oksit yarı iletken (CMOS) 2 boyutlu görüntüleme sensörü, 15 km'den daha iyi bir görüntü şerit genişliği sağlamak için seçilmiştir. Hizalama ve optik üretimle ilgili sınırlamaları belirlemek için optik tasarımın tolerans analizi yapılmıştır. Elektro-optik kamera tasarımının performansını göstermek için modülasyon transfer fonksiyonu (MTF) ve sinyal-gürültü oranı (SNR) bütçeleme analizleri de gerçekleştirilmiştir.

Anahtar Kelimeler: Küpsat, optik tasarım, tolerans analizi, telefoto optik sistem, elektro-optik kamera.

"Dedicated to my family"

ACKNOWLEDGEMENTS

To everyone who contributed to making this thesis a reality, I would want to convey my sincere gratitude and appreciation. The work would not have been accomplished without their assistance, direction, and encouragement.

First and foremost, Prof. Dr. Ahmet Bingül and Dr. Özgür Karcı, who served as my thesis advisers, have my sincere gratitude for all of their guidance, expertise, and patience. This research and my academic development are greatly influenced by their mentoring and invaluable insights.

In addition, I would like to express my gratitude to Prof. Dr. A. Necmeddin YAZICI and Prof. Dr. Koray KÖKSAL, who served on my thesis committee. Their insightful feedback and constructive critiques greatly improved the quality of my work.

I would like to thank TÜBİTAK Space Technologies Research Institute, the institution where I worked while completing my thesis, for allowing me to carry out this study. I express my gratitude to Mustafa Ekinci for his unwavering support and extensive technical expertise.

My sincere appreciation is extended to the study participants, without whom this research could not have been carried out. We truly appreciate their willingness to share their experience and insights.

My sincere gratitude goes out to my dear spouse Yalçın Yazgan, who has supported me during the thesis writing process. I sincerely appreciate his unwavering love, support, and encouragement. I respect him for being always an inspiration to me. I consider it an amazing blessing to have him in my life.

I would like to thank my father—Ömer Konaklı, and my mother—Zübeyde Konaklı, for their constant encouragement and support during my academic studies. I am grateful to my three beautiful sisters, Kübra, Verda, and Aysude, who inspire and faith in me endless motivation. To have such an amazing family at my side makes me feel lucky.

I am appreciative of the constant presence and support of my loving spouse's parents, Zinnure and Mahmut Yazgan, as well as their brother, Sinan Yazgan, during this trip. I am grateful for their continued encouragement and kindness toward me.

I am deeply thankful to my friends and colleagues who provided valuable input, offered a listening ear, and shared the ups and downs of this thesis adventure. I would especially like to thank my dear friends Dr. Sera İflazoğlu, Meltem Yeşiltepe, Dr. Zeynep Nilüfer Öztürk, Eray Arpa, and Serdar Şengül.

This thesis is the result of several years of work, dedication, and support from many people. I want to thank everyone for helping to make this academic achievement possible.

TABLE OF CONTENTS

Page

LIST OF TABLES

Page

LIST OF FIGURES

Page

LIST OF SYMBOLS

A_s	Photosensitive area of the sensor
A	Clear aperture area
a	Front lens group-positive
b	Rear lens group-negative
D	Clear aperture
d	Distance between the front and the rear lenses
$\mathbf{d_{opt}}$	Optimum distance between the lenses
$\mathbf{d_\lambda}$	Spectral sampling distance
f	Effective focal length
f_a	Focal length of the front group a
f_b	Focal length of the rear group b
f/#	F-number
f_N	Nyquist frequency
G	Gravitational constant
H	Position in the image field
H	Horizontal size of the sensor in μm
H'	Horizontal size of the sensor in mm
h	Orbit height
ℏ	Object height
h'	Height of the image plane
h'_p	Paraxial height of the image plane
í	Half of the sensor's diagonal size
I_λ	Dark current
k	Telephoto factor
L	Total system size
$L(\lambda)$	Spectral radiance
M	Mass of the Earth

$\mathbf{n_d}$	Refractive index
$\boldsymbol{N_{bits}}$	Quantization
$\boldsymbol{N_{FWC}}$	Full well capacity
$\boldsymbol{p}$	Pixel size
Q	Q number
$\boldsymbol{r}$	Radius of the Airy disk
$\boldsymbol{R}$	Radius of the Earth
$\boldsymbol{S_{total}}$	Imaging signal
s	Back focal length
$\boldsymbol{s}$	Swath width
t	Center thickness of the optical element
$\boldsymbol{\tau_F}$	Transmittance of the sensor filter
$\boldsymbol{\tau_T}$	Optical transmittance value
$\mathbf{T_g}$	Transformation temperature
$\boldsymbol{V}$	Vertical size of the sensor in μm type
$\boldsymbol{V'}$	Vertical size of the sensor in mm type
$\mathbf{V_d}$	Abbe value
$\boldsymbol{W}$	Third-order wave aberration equation
$\boldsymbol{W_{040}}$	Third-order spherical aberration coefficient
$\boldsymbol{W_{131}}$	Third-order coma coefficient
$\boldsymbol{W_{222}}$	Third-order astigmatism coefficient
$\boldsymbol{W_{220}}$	Third-order field curvature coefficient
$\boldsymbol{W_{311}}$	Third-order distortion coefficient
WFE	Wavefront error
$\boldsymbol{y_i}$	Field height
$\mathbf{z_i}$	The position of the axial
ρ	Density
$\boldsymbol{\rho}$	The height in the exit pupil
Λ	Thermal conductivity
$\boldsymbol{\alpha_{-30/+70}}$	The coefficient of thermal expansion in the temperature range between – 30°C and + 70°C
$\Delta\boldsymbol{\lambda}$	Spectral range
$\boldsymbol{\lambda}$	Spectral band (wavelength)

$\boldsymbol{\lambda_{BW}}$	Bandwidth of the sensor filter
$\boldsymbol{\lambda_{ref}}$	Reference wavelength
$\boldsymbol{v_0}$	Orbital velocity
$\boldsymbol{v_g}$	Ground velocity
$\boldsymbol{t_s}$	Exposure time
$\boldsymbol{\sigma_i}$	Individual noise source for the imaging sensor
$\boldsymbol{\sigma_{dark}}$	Dark noise
$\boldsymbol{\sigma_{quan}}$	Quantization noise
$\boldsymbol{\sigma_{read}}$	Readout noise
$\boldsymbol{\sigma_{shot}}$	Shot noise
$\boldsymbol{\sigma_{total}}$	Total noise
$\boldsymbol{\Omega}$	Solid angle
$\boldsymbol{\emptyset}$	Angle difference between the paraxial chief ray and the real chief ray

LIST OF ABBREVIATIONS

ASTI	Third-order astigmatism aberration
CMOS	Complementary metal-oxide semiconductor
COMA	Third-order coma aberration
COMP	Thickness, radius, or conic compensator command
CPAR	Parameter as a compensator command
DIST	Third-order distortion aberration
FCUR	Third-order field curvature aberration
FF	Fill factor
FFD	Full Field Display
FFOV	Full Field of View
GSD	Ground Sampling Distance
HFOV	Half Field of View
LDE	Lens Data Editor
LEO	Low Earth Orbit
LWIR	Long wavelength infrared
max	Maximum levels of image intensity
min	Minimum levels of image intensity
MC	Monte Carlo
MTF	Modulation Transfer Function
$\mathbf{MTF_{system}}$	System Modulation Transfer Function
$\mathbf{MTF_{atmosphere}}$	Atmosphere Modulation Transfer Function
$\mathbf{MTF_{optics}}$	Optics Modulation Transfer Function
$\mathbf{MTF_{detector}}$	Detector Modulation Transfer Function
$\mathbf{MTF_{satellite}}$	Satellite Modulation Transfer Function
NIR	Near-infrared
QE	Quantum efficiency
QE(λ)	Spectral quantum efficiency

RGB	Reg, green, blue
RSS	Root sum square
SNR	Signal-to-Noise Ratio
SPHA	Third-order spherical aberration
SWIR	Short wavelength infrared
SZA	Sun Zenith angle
TDE	Tolerance data editor
TED	Decenter error tolerance
TET	Tilt error tolerance
TEZI	Tolerance on surface irregularity
TOTR	Total length
TRAD	Tolerance on radius
TTHI	Tolerance on thickness

CHAPTER I

INTRODUCTION

"CubeSat" is a compound word formed from two meaningful components: 'cube' and 'satellite', which logically denote cube satellites. Two professors, Jordi Puig-Suari of California Polytechnic State University and Bob Twiggs of Stanford University developed CubeSat standards. This concept was introduced in 1999 to engage university students in spacecraft design, testing, and operation. The inaugural CubeSat depicted in Figure 1.1 was launched in 2003, while the first NASA CubeSat, GeneSat-1, was successfully launched in 2006, significantly boosting the popularity of CubeSats [1].

Until 2013, CubeSats primarily serviced restricted areas like academic and educational institutions. After this time, though, they started being used more often in commercial and amateur CubeSat projects. The variety of uses for these satellites is growing with each passing year [2].

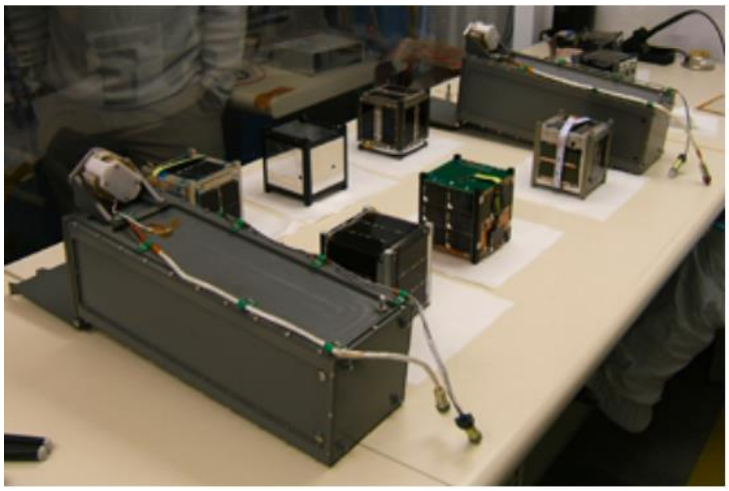

Figure 1.1 The first-ever CubeSat in May 2002 on a Kosmotras, Dnepr ELV from Bikinour, Ukraine.

CubeSats, typically operating in Low Earth Orbit (LEO), between 400 – 800 km, serve various purposes, including imaging, atmospheric research [3], biological studies [4],

climate assessment, or scientific research. The primary goal of the CubeSats is reducing costs, accelerating the development timelines, enhancing access to the space, minimizing the risks to the launch vehicle, and maintaining regular launch schedules [5]. The main reason behind the popularity of CubeSats is their affordability and compact sizes [6].CubeSats are designed for these applications to adhere to specific dimensional constraints. The standard size of a CubeSat is 100 mm x 100 mm x 100 mm, referred to as 1U. Over time, larger sizes have been developed. 1U CubeSat has a mass of approximately 1.33 kg (3 lbs). CubeSats can range from 1U up to 36U (336 x 336 x 450 mm^3) [7], as illustrated in Figure 1.2. Moreover, the satellites are classified according to their mass [8] as depicted in Table 1.1. CubeSats can be categorized into the group of nano or microsatellites.

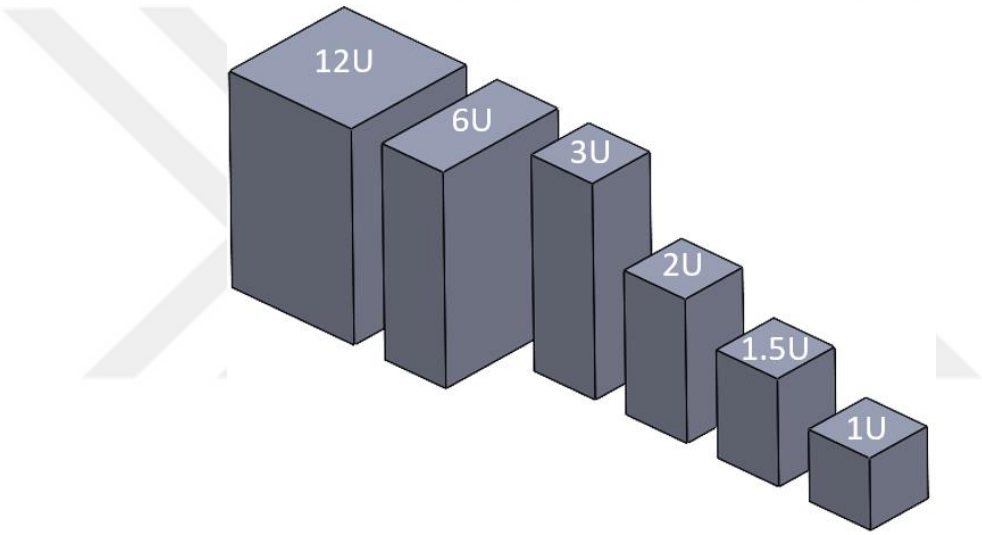

Figure 1.2 The CubeSat Group sizes in the standard.

Table 1.1 Satellites classified by mass.

Parameters	**Mass**
Large satellites	> 1000 kg
Medium satellites	500 to 1000 kg
Small satellites	< 500 kg
- Mini satellites	100 to 500 kg
- Microsatellites	10 to 100 kg
- Nanosatellites	1 to 10 kg
- Picosatellites	100 g to 1 kg

CubeSats fall under the category of nanosatellites, and below are the standard dimensions for CubeSats [8]:

- 1U CubeSat is 100 mm x 100 mm x 113.5 mm.
- 2U CubeSat is 100 mm x 100 mm x 227 mm.
- 6U CubeSat is 200 mm x 100 mm x 340.5 mm.
- 12U CubeSat is 200 mm x 200 mm x 340.5 mm.

CubeSats are also preferred and designed for Earth observation. Earth observation is a field of science that uses data from spacecraft or other high-altitude platforms to study Earth's surface, atmosphere, and other environmental aspects. Electro-optic cameras provide the data for these observations. For that purpose, electro-optics cameras are used as payloads. Large areas of the Earth's surface are potentially observed simultaneously thanks to satellite-based observations. The image in Figure 1.3 is an example of a satellite image captured by İMECE (launched by TÜBİTAK Space Technologies Research Institute in April 2023), the first domestically developed and nationally owned Earth observation satellite within the class of medium satellites [9].

Figure 1.3 İMECE satellite image with 0.98 m ground sampling distance.

Satellite systems like Sentinel [10] or the Landsat [10] series provide images that are utilized for various purposes, such as tracking changes in the forest cover and monitoring agricultural regions. The most preferred purposes of satellite imaging systems are listed below.

Environmental Monitoring: Used for tracking natural catastrophes, keeping monitors on forest fires, and managing water supplies, among other environmental uses.

Agriculture and Soil Management: Used in soil quality assessment, irrigation management, productivity enhancement, and monitoring of agricultural regions.

Urban Planning: Provides information for infrastructure projects and is used to track the expansion and transformation of urban areas.

Air Quality Monitoring: Evaluate the air quality by observing variations in the atmosphere.

Sea and Ocean Observation: Used to track variables including water pollution, changes in sea level, and sea surface temperatures.

Satellites are categorized according to different uses, and each has distinct features. Wavelength is a clear standout in these features, especially regarding application relevance. This classification, based on where the satellites are in the electromagnetic spectrum, underlines the usefulness of space-based images for specific applications. Specialized space imaging systems are built on various wavelengths, from visible light to microwaves, covering a wide range of applications from atmospheric monitoring to plant health and military purposes. Panchromatic (mono) imaging in the visible spectrum, such as 450-800 nm, is the most common imaging scenario for Earth observation platforms. In addition, multispectral imaging in the visible spectrum, such as RGB+NIR (red, green, blue, and near-infrared) and hyperspectral imaging between 400-2500 nm with about 10 nm spectral resolutions, are also common alternative applications for Earth observation. The electromagnetic spectrum categorization of satellites enables each satellite to provide optimal performance suited to a particular application purpose as shown in Figure 1.4 [11].

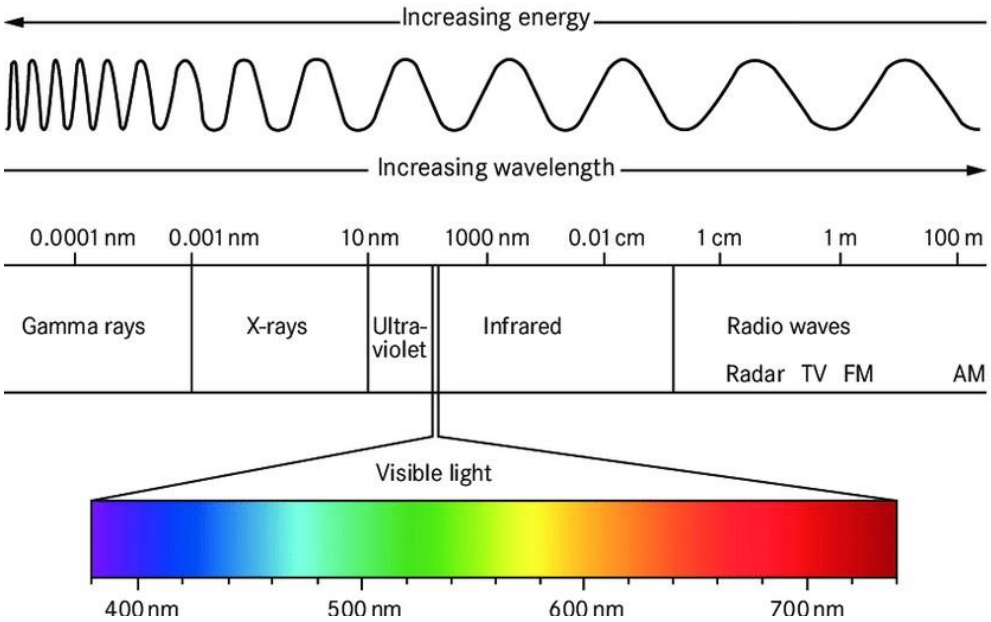

Figure 1.4 Schematic description of the electromagnetic spectrum [12].

Many CubeSats have been designed with the purposes mentioned above and features. Table 1.2 contains a list of successful launches and operations dedicated to satellite

observation for CubeSats. Examining the sample CubeSat models listed in Table 1.2 reveals ten products in three RGB, two video RGB, two hyperspectral, and two multispectral bands. The items on the market of Simera Sense firm are modified Cassegrain optical design, whereas the products of Cosine Remote Sensing B.V. - HyperScout® 1 and Cosine Remote Sensing B.V. - HyperScout® M are hyperspectral design products, according to the information obtained. The abbreviation used in Table 1.2, Δλ, GSD, *s*, *f*, *D*, and FFOV express spectral range, ground sampling distance, swath width, effective focal length, clear aperture, and full field of view respectively (The across track value is shown by the FFOV value in the table).

Table 1.2 The CubeSats spaceborne imagers for Earth observation.

CubeSat Model	**Δλ (nm)**	***GSD* (m)**	***s* (km)**	***f* (mm)**	***D* (mm)**	***FFOV***	**Size**
Simera Sense-HyperScape100	450-900 (32 bands)	4.75	19.4	580	95	2.22°	>3U
Simera Sense-MultiScape100 CIS	450-900 (7 bands)	4.75	19.4	580	95	2.22°	>3U
Simera Sense-MultiScape200 CIS	450-900 (7 bands)	1.5	14	1067	190	1.6°	>12U
Simera Sense-TriScape100	450-670 (Video)	4.75	19.4	580	95	2.22°	>3U
Simera Sense-TriScape200	450-670 (RGB/Video)	1.5	14	1067	190	1.6°	>12U
KAIROSPACE	RGB, PAN (Up to 6 bands)	3.75 (PAN) 6.25 (Color)	12.5	500	90	1.5°	>6U
KAIROSPACE	RGB, PAN (Up to 6 bands)	30.8 (Color)	104	76.5	22	12°	>1U
KAIROSPACE	RGB, PAN (Up to 32 bands)	30.8 (Color)	94.9	76.5	22	12°	>1U
Cosine Remote Sensing B.V.-HyperScout® 1	450-950	67	280	41.25	10.3	31°	>1U
Cosine Remote Sensing B.V.-HyperScout® M	450-950	55	225	50	12.5	25°	>1U

The optical designs of electro-optic cameras for Earth observation are based on refractive optics [13], catadioptrics [14], or reflective optics [15]. Refractive optical designs are preferred especially for small aperture size electro-optic cameras such as 1U size due to the lack of obscuration, ease of the alignment process of lenses, and the costs. The refractive optical design targeted for the system not only meets the specified criteria but also offers additional advantages, including a compact structure, small volume, and a smaller size than the effective focal length of the system.

Telephoto-type optical systems are one of the most suitable designs for long-distance imaging such as Earth observation for CubeSats. Telephoto optical system designs are typically used for ground observation in the literature, and their effective focal lengths are usually short. However, refractive optical design designs suitable for the space environment are relatively rare and find applications in imaging satellite platforms.

The optical specification parameters of similar studies conducted for Earth observation are given in Table 1.3. Gao *et al.* guided on creating an athermalized telephoto object of the long wave infrared type that is impervious to intense fog. Dong *et al.* described a dual-band refractive-diffractive telephoto lens with a long effective focal length and a wide variety of athermalized pathways that has been the subject of a theoretically and programmatically designed investigation, based on the concept of passive optical athermalization. In Mu *et al.*'s work, the 200 mm effective focal length design is implemented in the JTC dual-band infrared coaxial telephoto objective research. In Xu *et al.*'s work, the team constructed an infrared telephoto with an aspherical surface to improve the target recognition ratio and target detection range. In Dong *et al.*'s article, the goal of the project is to improve JTC's target tracking and recognition capabilities by designing an infrared telephoto lens with refraction, a long effective focal length, a large diameter, and athermalization. In the Gardner's study, looks at the difficulties and solutions associated with designing high-performance SWIR telephoto lenses. In Şahin's study, the design used in this investigation is intended to function in the 0.4 µm–1.1 µm wavelength range. It includes an evaluation of the design's outcomes. Yu *et al.* established the basis for developing a large relative aperture cooled LWIR telephoto optical system using the passive optical athermalization technique. *f/#*, λ, and D_R represent F-number, spectral band, and relative aperture in Table 1.3.

Table 1.3 Refractive optics based on telephoto design.

Name of Study	*f*/#	D_R	*f* (mm)	*FFOV*	λ (µm)
Gao et al. [16]	*f/2*	-	150	6°	8-12 µm
Dong et al. [17]	-	1:2.2	200	7°	3-5 µm, 8-12 µm
Mu et al. [18]	-	1:3	200	-	3-5 µm, 8-12 µm
Xu et al. [19]	-	1:2.6	200	6°	8-12 µm
Dong et al. [20]	-	1:3	200	6.4°	8-12 µm
Gardner et al. [21]	*f*/1.4	-	25	55.2°	-
Şahin. [22]	*f*/2.3	-	57.5	7.8°	0.4-1.1µm
Yu et al. [23]	*f*/2	-	100	7°	8-12 µm

Refractive electro-optic camera based CubeSats have recently been the most preferred for Earth observation because of their versatility, affordability owing to their small size, and ability to be designed in different spectral bands. Table 1.3 reveals that the optical design of *Gao et al., Dong et al., Mu et al., Xu et al., Dong et al., Gardner et al., Şahin,* and *Yu et al.* is refractive based. The studied products in the literature have focal lengths of less than 200 mm and are mainly intended for use in ground observation for military applications. Based on these investigations, no research has been identified on the use of materials resistant to space radiation in optical design for Earth observation. A wide-angle, long focal length, low-cost telephoto optical system is studied to enhance this field in the literature.

An electro-optic camera concept for low Earth orbit (LEO) Earth observation is presented in this thesis, which is designed to fit into a 6U CubeSat platform. In CHAPTER II, system engineering calculations for a CubeSat mission are presented according to the mission requirements, and the prerequisites for achieving the optical design are defined. At 400 km altitude, the design aims to attain a ground sampling distance (GSD) of 4.5 m. The camera's optical design is built for a refractive, telephoto objective architecture made up of six spherical lenses using space-compatible optical materials. Using ray-tracing software (i.e. OpticStudio), an F/5.5 telephoto objective with near diffraction-limited performance spanning 2.6 degrees of the full field of view

(FFOV) is adjusted for panchromatic imaging in the 450–700 nm range. To achieve a swath width of more than 15 kilometers, a commercial complementary metal-oxide semiconductor (CMOS) 2-D image sensor is chosen. The designed electro-optic camera's modulation transfer function (MTF) value is better than 0.1. The design and tolerance analysis of the optical system is covered in CHAPTER III. To identify constraints on alignment and optical manufacturing, a tolerance analysis of the optical design is conducted. To demonstrate the performance of the electro-optic camera design, a budget analysis for the modulation transfer function (MTF) and signal-to-noise ratio (SNR) are also carried out in CHAPTER IV and CHAPTER V.

CHAPTER II

SYSTEM ENGINEERING

Optical design parameters are determined based on the system requirements of a specific CubeSat-based Earth observation mission. The optical performance of the electro-optic system, which depends on critical characteristics including the modulation transfer function (MTF), signal-to-noise ratio (SNR), and ground sampling distance (GSD) is greatly influenced by these parameters.

In this chapter, the relationships among the design parameters of the electro-optic system are elucidated, and the optical system design parameters are determined. The chapter provides information about the effective focal length (*f*), full field of view (FFOV), clear aperture (*D*), and F-number (*f/#*) of the optical system, all of which are calculated according to the system requirements.

2.1 System Requirements

The requirements provided by the mission hold significant importance in the design of a system and serve as a roadmap for developing an electro-optic camera. This thesis details the process of preparing the system design based on the requirements outlined in Table 2.1.

Table 2.1 System requirements for the mission.

Parameters	**Symbol**	**Value**
Orbit Height	*h*	400 km
Ground Sampling Distance	*GSD*	≤ 4.5 m
Swath Width	*s*	≥ 15 km
Spectral Band (Mono)	*λ*	450-700 nm
Electro-optic camera's *MTF*	*MTF*	> 0.1
Signal-to-Noise Ratio	*SNR*	> 75
Total Length	*TOTR*	< 400 mm
Clear aperture	*D*	< Ø100 mm

The first step of the system engineering for an electro-optic camera development is selecting a proper imaging sensor according to the mission requirements. Imaging

sensor specification is a leading input for an optical design. The CMV12000 12-megapixel complementary metal-oxide semiconductor (CMOS) type imaging sensor is selected as the imaging sensor for the mission [24]. The specifications of the sensor are listed in Table 2.2.

Table 2.2 Specification of the Osram CMV12000 CMOS Image Sensor.

Parameters	**Symbol**	**Value**
Detector Type	-	CMOS
Pixel Pitch	p	5.5 µm
Spectrum	λ	450 - 700 nm
Quantum Efficiency (@500 nm)	QE	>46%
Dimension	Pixel x Pixel	4096(H) X 3072 (V)
		22.5(H') X 16.9 (V')
Readout Noise	σ_{read}	13 ē
Full Well Charge	N_{FWC}	13,500 ē
Modulation Transfer Function	MTF	58%

The Quantum efficiency (QE) of the CMOS sensor, which represents the ratio of the number of incident photons that are transformed into electrons concerning the wavelength, is given in Figure 2.1.

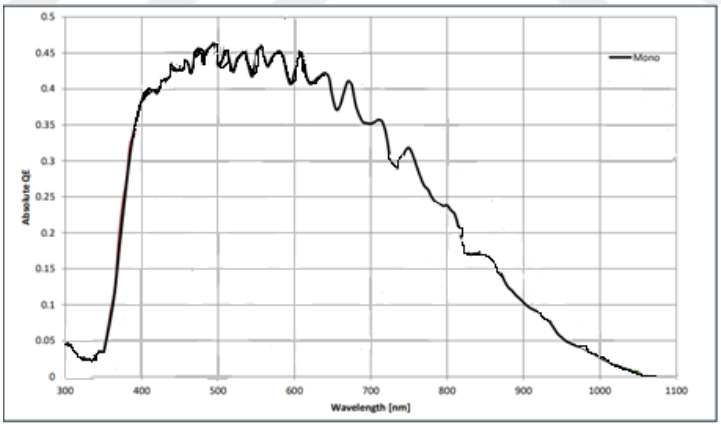

Figure 2.1 Quantum efficiency graph of the Osram CMV12000.

2.2 Calculation of the Optical System Parameters

The effective focal length, full field of view, clear aperture, F-number, and swath width have all been calculated as design parameters for the optical system. Each of these parameters is evaluated in the following.

2.2.1 Effective Focal Length

The system's effective focal length is calculated after selecting the imaging sensor, as shown in Figure 2.2. The system's effective focal length, f, is calculated using the equation below.

$$f = \frac{h * p}{GSD} \tag{2.1}$$

where *h*, *p*, and *GSD* are orbit height, pixel size, and ground sampling distance, respectively. f is computed as 500 mm for the system requirements listed in Table 2.1 and Table 2.2.

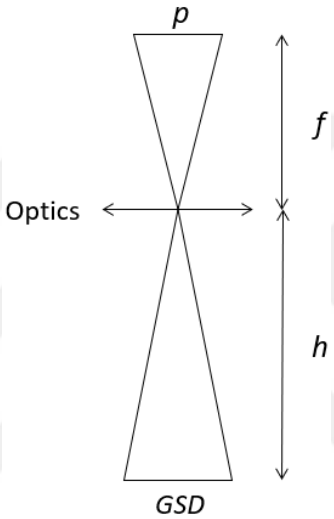

Figure 2.2 Schematic description of the ground sampling distance (GSD) which shows the projection of a pixel on the ground through the optics.

2.2.2 Full Field of View

The full field of view (FFOV) describes the electro-optic camera system's whole field of view. The image plane of the camera must be at least as large as the sensor's diagonal to provide a diffraction-limited illumination of the full image sensor surface. As shown in Figure 2.3, the circular area represents the fully illuminated area, and the square area represents the sensor's diagonal dimension (*2*ί). The sensor's diagonal dimension is calculated as

$$\acute{\imath} = \sqrt{\left(\frac{H'}{2}\right)^2 + \left(\frac{V'}{2}\right)^2} \tag{2.2}$$

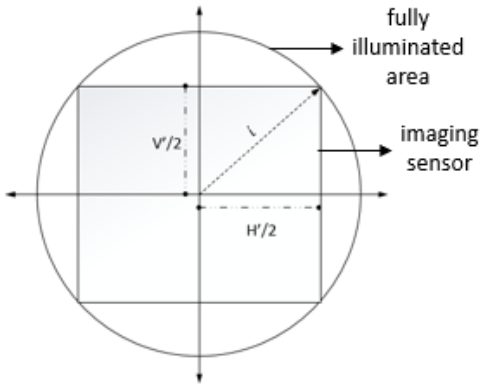

Figure 2.3 Schematic illustration of the sensor's diagonal size and illuminated area on the image plane of the electro-optic camera.

where ί, H', and V' are half of the sensor's diagonal dimension, horizontal size of the sensor, and vertical size of the sensor, respectively. The sensor's diagonal dimension is calculated to be 28.16 mm. Half of the optical system's full field of view is referred to as the half field of view (HFOV*)* [25], which is calculated as

$$HFOV = tan^{-1}\left(\frac{2ί}{2f}\right) \tag{2.3}$$

where ί and f are half of the sensor's diagonal dimension, and effective focal length, respectively. HFOV is calculated to be 1.29°.

2.2.3 Swath Width

When a satellite scans the Earth from space, it gathers the light from a specific surface region of the surface. The area that the satellite scans, as shown in Figure 2.4, is represented by the swath width (s). The swath width is calculated as

$$s = 2 * h * tan(HFOV) \tag{2.4}$$

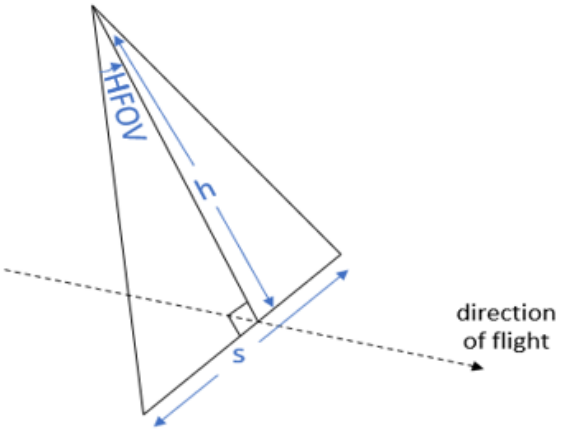

Figure 2.4 Schematic description of the swath width.

where *h* and *HFOV* are orbit height and half of the optical system's full field of view, respectively. The swath width is computed as 18 km for the corresponding system parameter.

2.2.4 Aperture and F-number

The Airy Disk is a physical in optics. Owing to the wave nature of light, light passing through an aperture is diffracted and forms a pattern of light and dark regions on a screen some distance away from the aperture. The diffraction pattern resulting from a uniformly illuminated circular aperture has a bright area in the center, known as the Airy disk which together with a series of concentric rings is called the Airy pattern [26] as shown in Figure 2.5. Less intense concentric rings surround the central disk, so light intensity takes local maxima and minima while it decreases away from the center. About 84% of the total light intensity is in the central disk, the remaining 16% is distributed in the concentric rings [27]. The diameter of this disk is related to the wavelength of the illuminating light and the size of the circular aperture. The Airy disk (r) is calculated using the equation below [28].

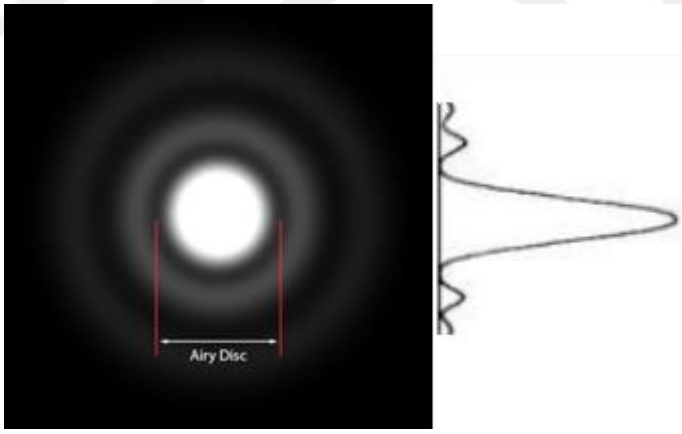

Figure 2.5 Schematic description of the Airy Disk in which 84% of the total energy is stored.

$$r = 1.22 * \lambda * f/\# \tag{2.5}$$

where λ and $f/\#$ are wavelength and F-number, respectively. The F-number is defined as

$$f/\# = \frac{f}{D} \tag{2.6}$$

where f and D are the effective focal length and clear aperture, respectively. D is computed as 63.77 mm when the λ value is set to 575 nm (mean value of the spectral bandwidth 450-700 nm) and the r value equals the pixel size of 5.5 μm. The SNR is another factor that affects the system's optimum clear aperture. The clear aperture is adjusted to 90 mm to satisfy the SNR requirement in Table 2.1 and collect more light from the Earth (in CHAPTER V).

2.2.5 System MTF

The most used metric for characterizing the optical system's performance is the MTF. It measures how well an optical system reproduces or transmits object information to the image it captures. A measurement of the transfer of contrast or modulation from the target object to the generated image is another definition for the MTF. The main metrics that MTF employs to measure the performance of the image are resolution and contrast [29]. The spatial frequency, or line-pair per millimeter (lp/mm), is the standard unit of measurement for resolution. A line pair consists of one black line and one white line. The difference between a black or dark line and a white or light line is called contrast. Stated differently, contrast or visibility is the degree to which the highest and lowest intensity values are transferred from the subject plane to the image plane. Equation 2.7 describes the contrast [30].

$$Contrast = \frac{max - min}{max + min} \tag{2.7}$$

where *max* and *min* are the levels of image intensity [31]. Thus, an optical system MTF measures its ability to transmit contrast from the object plane to the image plane at a certain resolution. As seen in Figure 2.6, an MTF graph shows the percentage of transmitted contrast as a function of resolution (lp/mm).

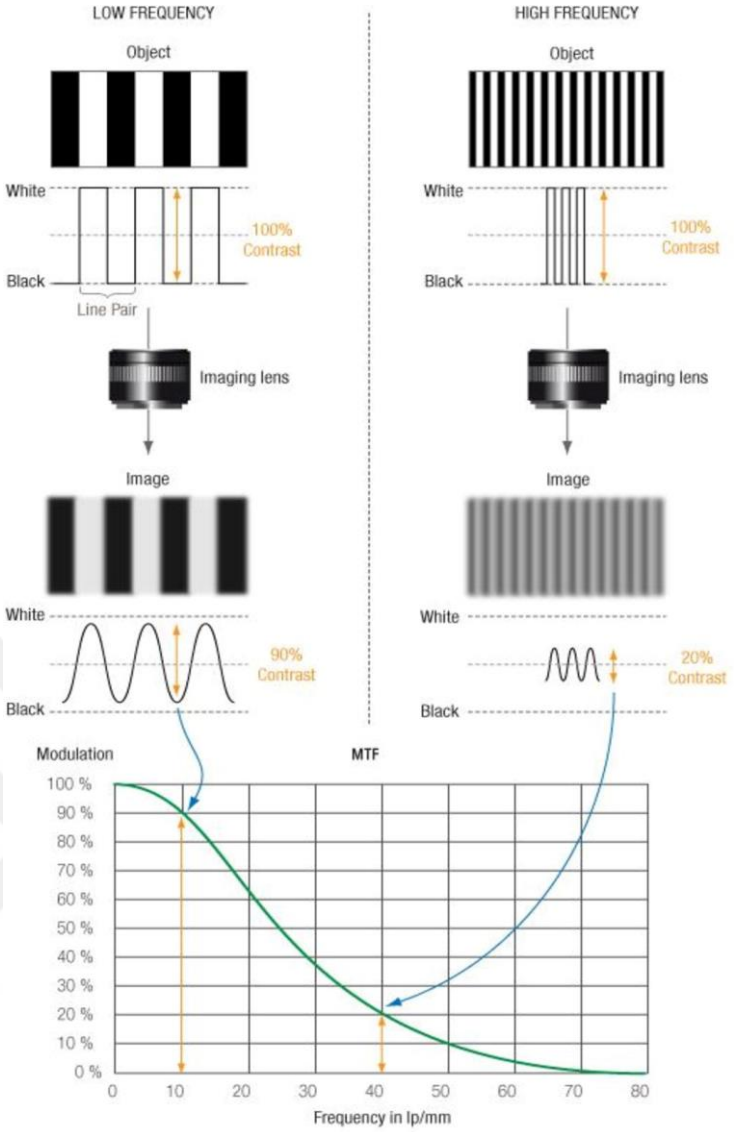

Figure 2.6 Illustration of MTF graph with various contrasts [32].

The Nyquist frequency, abbreviated as f_N and referred to as the sampling frequency, is another topic covered in this section. In a digital system, it represents the other half of the sampling rate. f_N is calculated as

$$f_N = \frac{1}{2 * p} \tag{2.8}$$

where p is the pixel size in mm of the sensor. For 5.5 µm pixel size, f_N is calculated to be 90 lp/mm. The performance of the MTF is subsequently evaluated using this value as a reference parameter.

Each factor influencing performance should be reviewed to determine the MTF budget of the system for satellite operation. As shown in Figure 2.7, the primary parameters that affect the system MTF are the satellite platform, atmosphere, optic, and imaging

sensor [33]. The system MTF is the convolution of these parameters and is calculated as,

$$MTF_{system} = MTF_{atmosphere} * MTF_{optics} * MTF_{detector} * MTF_{satellite} \quad (2.9)$$

In this study, the optic, and the imaging sensor, called the electro-optic camera as shown in Figure 2.7, are investigated and used for MTF budgeting.

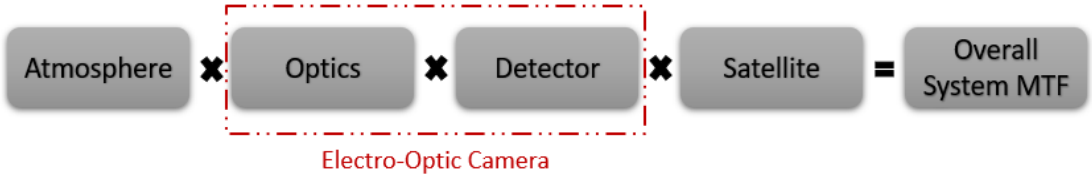

Figure 2.7 Calculation of the system MTF.

The impacts of the electro-optic camera system have been thoroughly examined within the parameters of this thesis. Thus, Considering the effect of all the parameters mentioned, the optical MTF is set as the target at 0.2 during the tolerancing step (including system realization, alignment, and manufacturing), assuming all parameters' MTF loss of 0.5 [34]. Considering the effect of all the parameters mentioned, the electro-optic camera's MTF (detector + optics) is 0.1. The goal of the tolerance analysis is the observation of the mean MTF.

Table 2.3 provides a summary of the optical system design parameters determined according to the mission requirements performing the system as mentioned above in engineering calculations.

Table 2.3 Overall optical system design parameters.

Parameter	Symbol	Value
Effective Focal Length	*f*	500 mm
Aperture	*D*	90 mm
F-Number	*f/#*	5.55
Full Field of View	*FFOV*	2.58°
Wavelength (Mean)	*λ*	575 nm
Modulation Transfer Function	*MTF*	>0.35

2.3 Optical Design

According to the determined system specifications, the refractive-based optical design is chosen considering the benefits of achieving a wide field of view, ease of alignment, no obscuration, and costs. A brief comparison is given in Table 2.4 between refractive

and reflective optical designs. In addition to the refractive design cost advantage given in Table 2.4, all elements in the optical design are built as spherical surfaces. Secondly, to achieve the required effective focal length, telephoto optical system architecture is considered for the optical design of the electro-optic system. The telephoto design offers a decent optical system length less than the effective focal length that is required.

Table 2.4 Comparison of the refractive & reflective design.

Parameter	**Refractive Design**	**Reflective Design**
Obscuration	No	Yes
Field of view	High	Low
Alignment Process	Easy	Hard
Length of the System	Tall	Short
Complicated Design (Limited material Options)	Yes	No
Cost	Cheap	Expensive

CHAPTER III

OPTICAL SYSTEM DESIGN

The optical system design parameters calculated in CHAPTER II are used to design the optical system utilizing commercial ray-tracing software (i.e. OpticStudio). The stages of the optical system's development and performance are described together. This phase ultimately performs a tolerance analysis of the completed optical system design.

3.1 Principle of the Telephoto Optical Design

Telephoto objectives are typically favored by photographers for taking photos from long distances. Their desire is primarily driven by its compact design, tiny volume, and system size that is less than the system's effective focal length. According to their effective focal length, telephoto systems may be divided into four basic categories. These are the four types of telephoto objectives: short, medium, long, and extreme [35]. Table 3.1 illustrates how various telephoto variations relate to system parameters with a detector of 35 mm size. As seen in Table 3.1, there is an inverse relation between the effective focal length and the full field of view.

Table 3.1 Optical parameter values for telephoto objectives [35].

Type	***f*** **[mm]**	***f/#***	***FFOV*** **(dia) [deg]**	**Architectural Design**	**Element Number**
Short	75-105	2.8	37	Double Gauss, Telephoto	5
Medium	120-200	4	21	Tessar, Telephoto	4-6
Long	300-500	8	8	Telephoto	4-7
Extreme	600-1200	11	4	Telephoto	2-5

Figure 3.1 displays the systematic diagram of photography lens setup families about aperture and field size. The telephoto objectives are classified as slow optics with a high F-number and a small FFOV as seen in Figure 3.1.

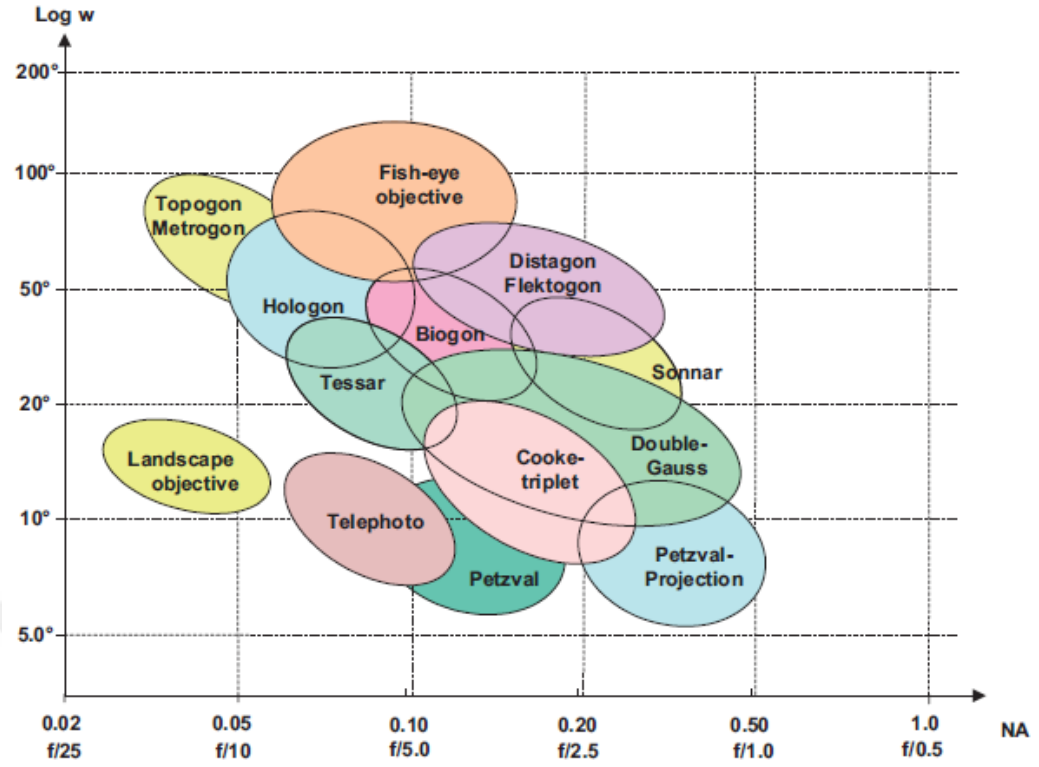

Figure 3.1 Families of photography lens setups organized according to the aperture and the field size [35].

In theory, telephoto optical design architectures are formed as double anastigmatic asymmetries. From the top of the first lens to the image plane, the total system size (*L)* is shown in Figure 3.2. The system's effective focal length is always greater than the system's physical size. Telephoto objectives are made up of both positive and negative lens groups. Positive lenses comprise the front group, designated as "a", while negative lenses comprise the back group, "*b*" [36].

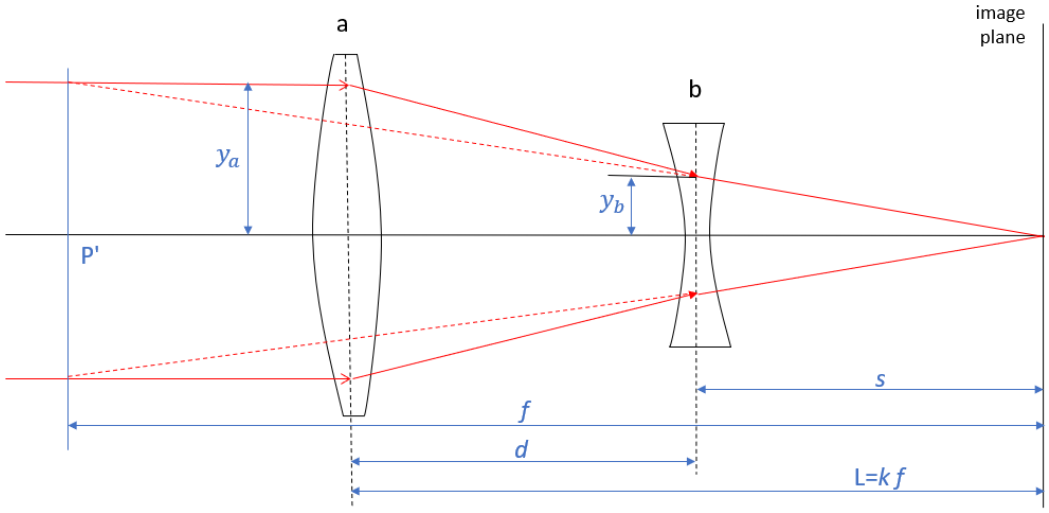

Figure 3.2 The basic concepts of the telephoto systems.

The focal lengths of the system's lenses are given in the equations below.

$$f_a = \frac{f * d}{f(1-k)+d} \tag{3.1}$$

$$f_b = \frac{(f_a - d)(kf - d)}{f_a - kf} \tag{3.2}$$

where, the front group's focal length is represented by f_a, and a. The focal length of the rear group is defined by f_b, and b. The distance between the front and back lenses is known as d. The equation below expresses the back focal length (s).

$$\mathrm{s} = kf - d \tag{3.3}$$

The telephoto ratio is one of the parameters used to classify telephoto optical systems. The telephoto factor, k, is the ratio of the system size to the effective focal length. This ratio occurs between the $0< k <1$ range and is determined using the equation below. This ratio can be decreased to reduce the system's size [37]. Usually, a telephoto factor value of about 0.8 is chosen [35].

$$k = \frac{\mathrm{L}}{f} \tag{3.4}$$

Figure 3.3 presents how this telephoto ratio affects the optical design element. The absolute value of f_b reaches its maximum near the halfway point of the system. The focal lengths of f_a and f_b are displayed as functions of distance for various telephoto factor values. All values are normalized to the system's effective focal length. The second zero of f_b and the yellow point represent the system length, respectively. To eliminate vignetting [38], which is described as reducing the brightness or saturation of an image from its center to its perimeter [39] as the distance grows, it becomes necessary to increase the lens diameters. The equation below expresses the optimum distance between the lenses, corresponding to the maximum value in the parabolic curve of f_b.

$$d_{opt} = {}^{L}/_{2} = {}^{k}/_{2} * f \tag{3.5}$$

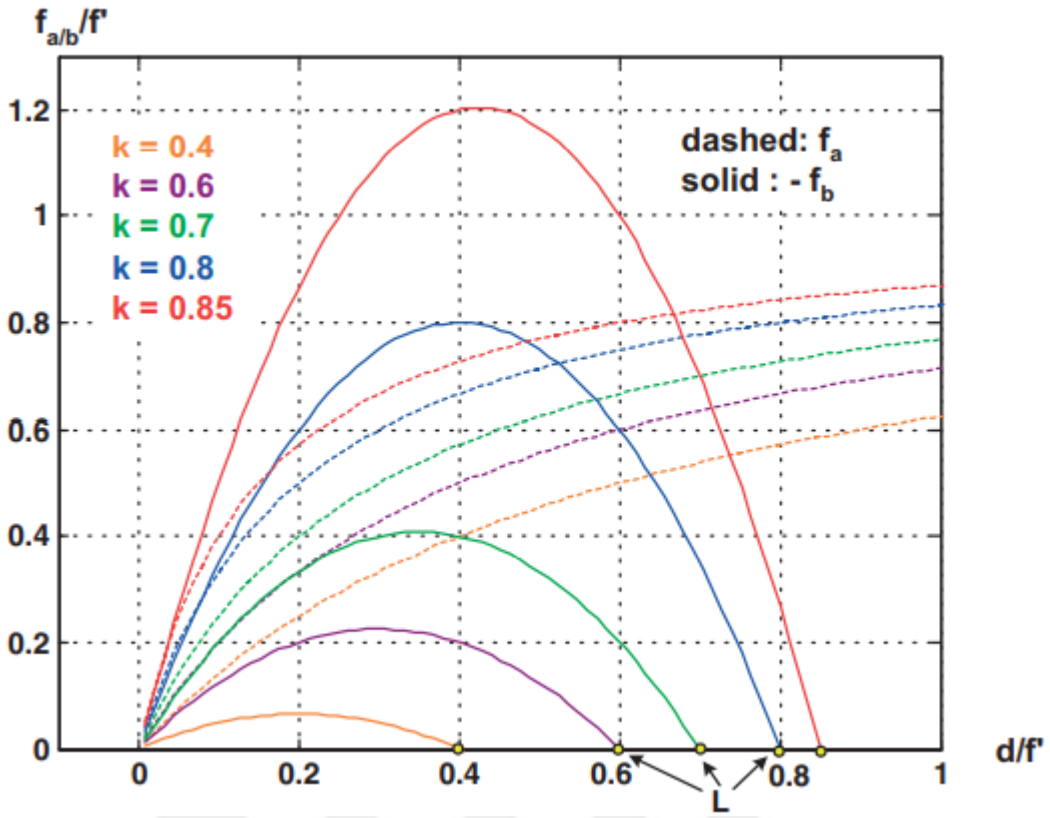

Figure 3.3 The relationship between the telephoto factor and the telephoto objective's effective focal length [35].

3.2 Optical Notions

Before introducing the subject of optical design aberrations, this section explains some basic optical concepts such as marginal, chief, and paraxial rays used in optical design and engineering. Light rays that go through an optical system in the direction of the lens aperture's edge, away from the optical axis, are known as marginal rays, as shown in Figure 3.4. The chief ray is defined as the ray originating from an off-axis point in the object and passing through the center of the aperture stop, as shown in Figure 3.4. Any ray that lies near the system's optical axis and forms a small angle with it is known as a paraxial ray as shown in Figure 3.5.

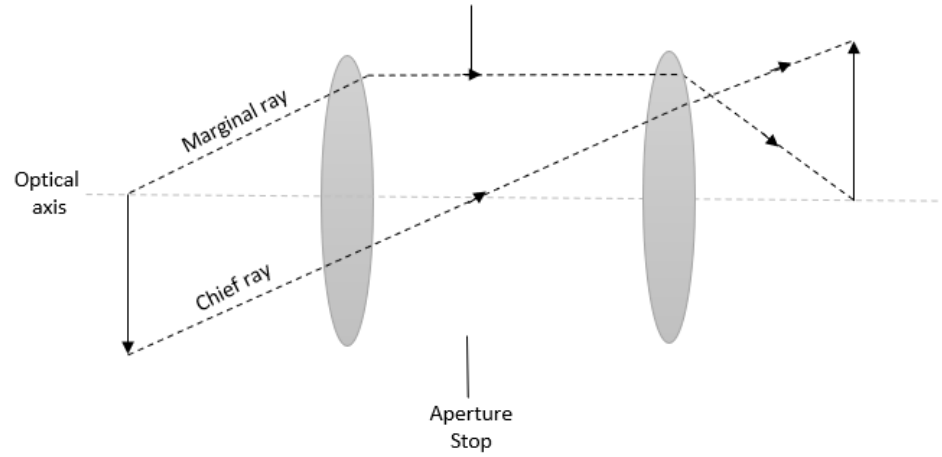

Figure 3.4 Schematic description of the marginal and chief rays.

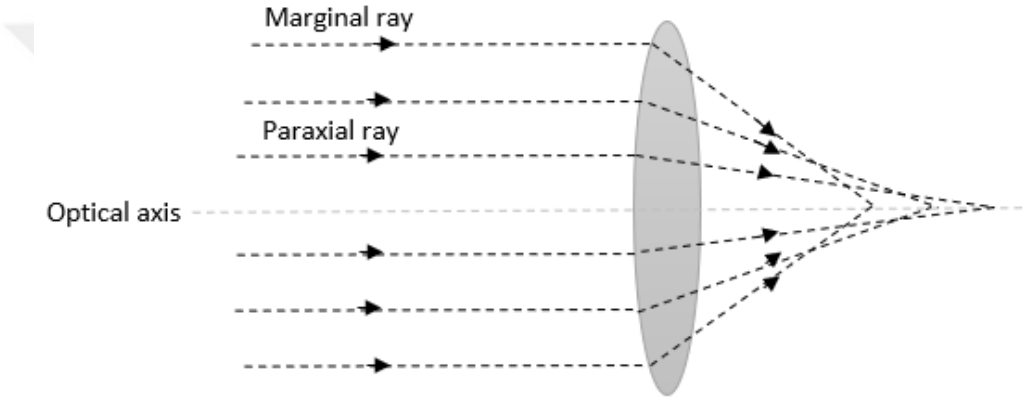

Figure 3.5 Schematic description of the paraxial and marginal rays.

3.3 Seidel Aberrations

The paraxial formulas once developed for the formation of images by spherical reflecting and refracting surfaces are only approximately correct. It was important to assume paraxial rays—that is, rays that are both close to and make small angles with the optical axis—to derive those equations. In terms of mathematics, the sine and cosine function power expansions are provided by

$$\sin x = x - \frac{x^3}{3!} + \frac{x^5}{5!} - .. \tag{3.6}$$

$$\cos x = 1 - \frac{x^2}{2!} + \frac{x^4}{4!} - .. \tag{3.7}$$

were, thus, roughly represented by the first terms. To the extent that these first-order approximations are valid. Gaussian optics implies accurate imaging. However, the derivations' inclusion of higher-order terms indicates that, as the angle increases, there

will be gradually larger departures from "perfect" imaging. "Aberrations" is the term used to describe these deviations. A result of third-order aberration theory is obtained when the subsequent term involving x^3 is included in the approximation for $\sin x$. The German mathematician Ludwig von Seidel examined and categorized the aberrations, now known as third-order or Seidel aberrations.

There are five Seidel aberrations for monochromatic light: spherical aberration, coma, astigmatism, field curvature, and distortion. Chromatic aberration is an additional aberration that results from an optical system's imaging qualities' wavelength dependency. Here, a brief description of how a third-order aberration leads to different abnormalities is presented [40]. The conventions for the field (H) and pupil (ρ) are represented in Figure 3.6. The third-order wave equation is represented by the symbol W [41].

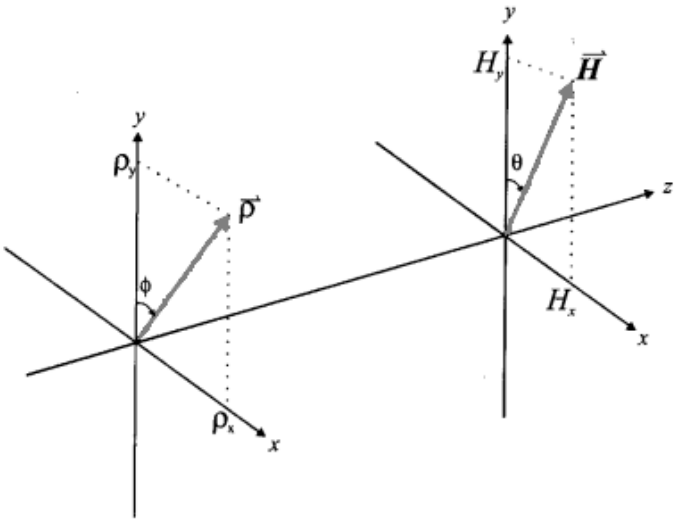

Figure 3.6 Conventions for the field vector H and pupil vector ρ [41].

$$W = W_{040}\rho^4 + W_{131}\hbar\rho^3\cos\phi + W_{222}\hbar\rho^2(\cos\phi)^2 + W_{220}\hbar^2\rho^2 + W_{311}\hbar^3\rho\cos\phi + \ldots\ldots, \qquad \theta = 0, \tag{3.6}$$

where, the $\hbar$ is the object height, the ρ is the height in the exit pupil position with ρ_x and ρ_y its components along x and y, the H represents the position in the image field with H_x and H_y its components along x and y. The W_{040} is the third-order spherical aberration coefficient, W_{131} is the third-order coma coefficient, W_{222}, is the third-order astigmatism coefficient, W_{220} is a coefficient involved in the third-order component of field curvature, and W_{311} is the third-order distortion [41] [42].

3.3.1 Third-Order Spherical Aberration

Third-order spherical aberration (SPHA) is described as the change of focus due to the aperture. The rays close to the optical axis (i.e., paraxial rays) are intersected the axis and come to focus. Since the height of the ray at the lens goes up, the position of the intersection of the ray on the optical axis becomes too far away from the paraxial focus. The effect of this situation is exemplified in Figure 3.7, where the position of the axial z_i rests on the field height y_i. The third-order spherical aberration has just aperture dependency with the forth order (ρ^4).

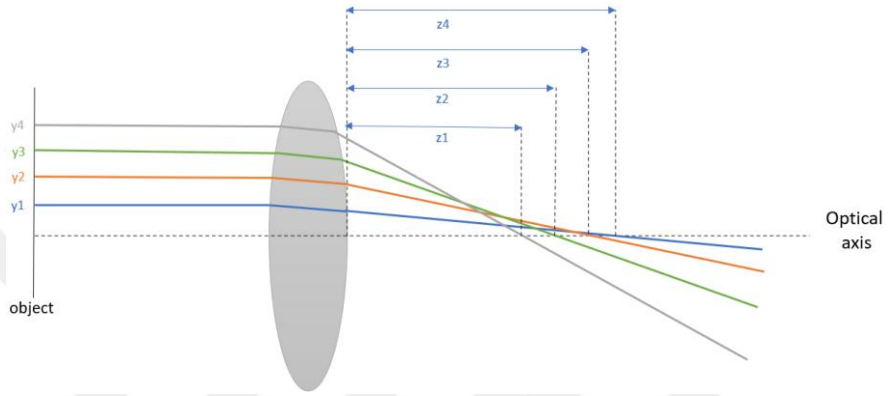

Figure 3.7 Schematic description of the third-order spherical aberration.

3.3.2 Third-Order Coma

Third-order coma (COMA) is where the circular zone of the aperture has variant magnification. Rays come from points not close to the principal axis. Then, these rays are focused on different places, and a comet pattern is formed on the image plane, as shown in Figure 3.8. This condition is called coma. The third-order coma has cubic aperture dependency (ρ^3), and linear field dependency ($\hbar$).

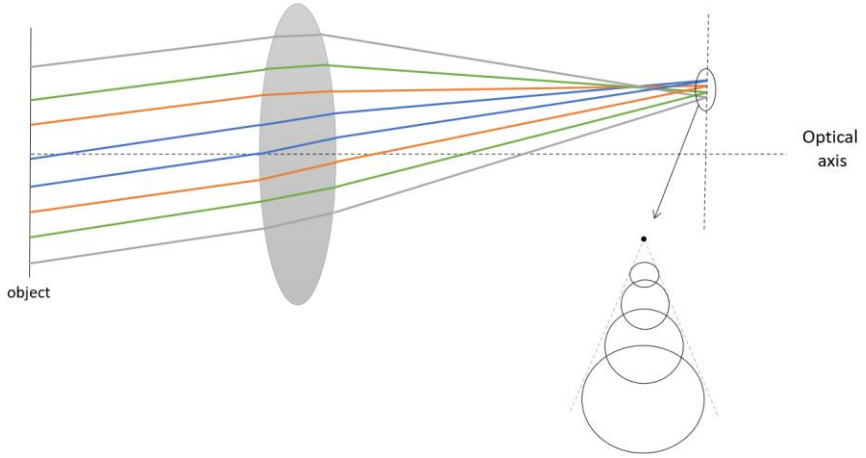

Figure 3.8 Schematic description of the third-order coma.

3.3.3 Third-Order Astigmatism

Third-order astigmatism (ASTI) is the aberration with tangential (meridional) and sagittal ray fans. Whenever off-axis rays come, these fans are focused on different locations as shown in Figure 3.9; the image does not coincide. Essentially, field curvature has a resemblance to astigmatism. The distinction between field curvature and astigmatism is that the magnitude of the aberration is dissimilar between x and y. The third-order astigmatism aberration has quadratic aperture and field dependency.

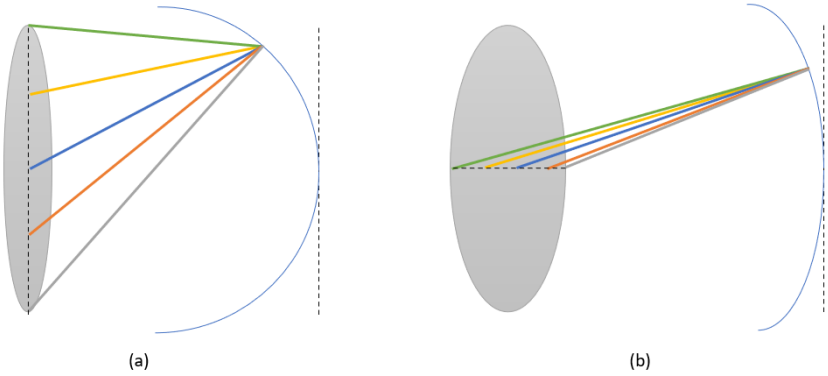

Figure 3.9 Schematic description of the third-order astigmatism (a) tangential, (b) sagittal.

3.3.4 Third-Order Field Curvature

Third-order field curvature (FCUR) is shown in Figure 3.10. In optical systems, rays must be focused straight on the image plane. Unfortunately, this is not always possible. In the case of field curvature in the optical system, the rays curve on the image plane. The third-order field curvature aberration has quadratic aperture and field dependency.

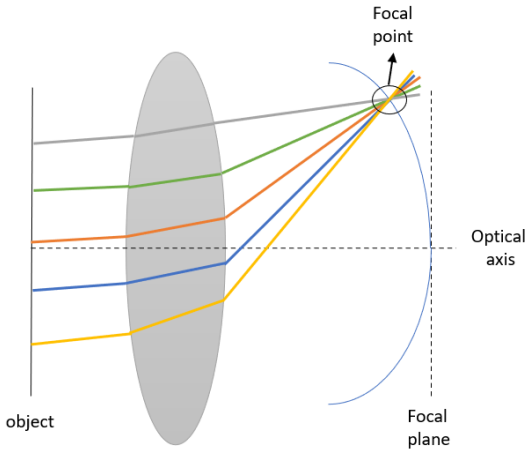

Figure 3.10 Schematic description of third-order field curvature.

3.3.5 Third-Order Distortion

Third-order distortion (DIST) can be described as a phenomenon in which the magnitude changes with the change in image height. As shown in Figure 3.11, magnification depends on the cube of the field, and changes with the angle difference between the paraxial chief ray and real chief ray (Ø). The third-order astigmatism aberration has linear aperture dependency and cubic field dependency. Distortion can be expressed as:

$$Distortion = \frac{h' - h'_p}{h'_p} \tag{3.7}$$

where, h' is the height of the image plane, h'_p is the paraxial height. Distortion induced by the optical system can be corrected by image processing and does not decrease the image quality.

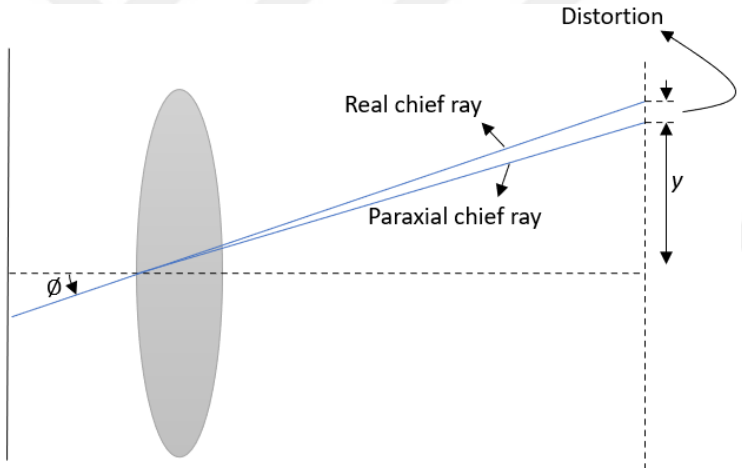

Figure 3.11 Schematic description of third-order distortion.

Distortion can be expressed as positive (pincushion) or negative (barrel) distortion as shown in Figure 3.12.

- Positive or pincushion distortion takes place in case of increasing magnification toward the edge of the field.
- Negative or barrel distortion takes place in case of decreasing magnification toward the edge of the field.

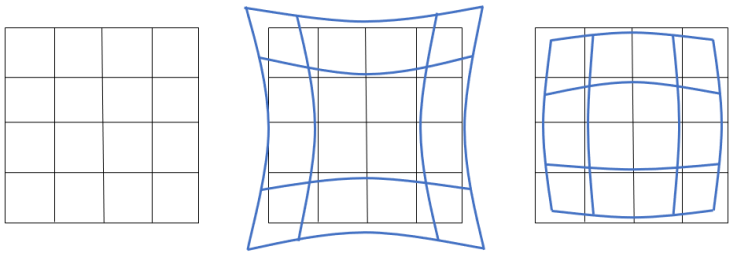

Figure 3.12 Schematic description of third-order distortion (a) zero, (b) positive or pincushion, (c) negative or barrel.

3.4 Optical Design Boundaries

The relationships between various system parameters while designing the system, are supplied in this subsection. The fixed system parameters listed in Table 2.3 are followed during the optical design phase. The differences in system size caused by various designs are evaluated about the modifications in system functionality.

The design criteria set out in CHAPTER II are used as guidance. Table 3.2 lists the design constraints considered when building the system design, as seen in Figure 3.14.

Table 3.2 Boundary conditions for the optical design.

Constrain	Value
Minimum lens separation	> 4 mm
Lens thickness	10-25 mm
Edge Thickness	4 mm
Material	Rad-hard

3.5 Optical Design

Based on the information from present optical designs, Figure 3.13 shows the graph that shows changes in the MTF, an essential element affecting the performance of the optical system, in response to changing telephoto factor values. As shown in Figure 3.13, the system size is just one variable, and all optical design data (field of view, effective focal length, F-number, wavelength) is kept constant. The average MTF value at Nyquist frequency, representing the design's performance, is determined for every stage. As the system size is reduced, there is a significant fall in the optical system MTF performance. According to the predetermined system requirements, the appropriate system size is selected. The system size ratio is chosen as 0.8.

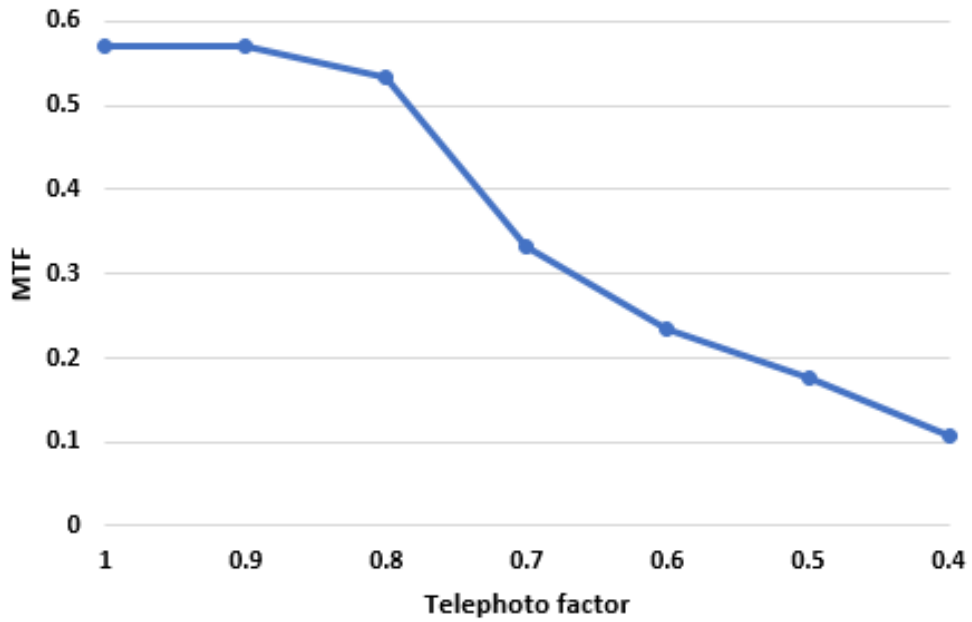

Figure 3.13 MTF as opposed to modifying telephoto factor values.

Two lenses—one positive and one negative—are used to start the optical design within the constraints given in Table 3.2 except that the rad-hard material. The system is then re-optimized when these lenses are converted into two cemented doublets to reduce the resulting aberrations. The stop stands at or nearest the front group for telephoto architecture [37]. Two additional lenses are added in both the third and fourth stages of the system design as the system's performance is insufficient. The system is re-optimized in the last stage, as shown in Figure 3.14 by adding an air space between the cemented doublets. It is important to note that using cemented doublets in a space environment is typically not recommended since the chemical adhesive possibly outgas [43]. The material itself produces pollution at the particle level. The transmission efficiency of the optical material gradually reduces due to this pollution's easy adhesion to the optical coating. As a result, over time, the optical system's performance has suffered markedly from this [44].

The thickness parameters are determined at a minimum of 10 mm, considering the lens manufacturing conditions [45]. Additionally, the edge thickness parameters are designed to maintain a minimum of 10 mm to consider mechanical holder tolerances.

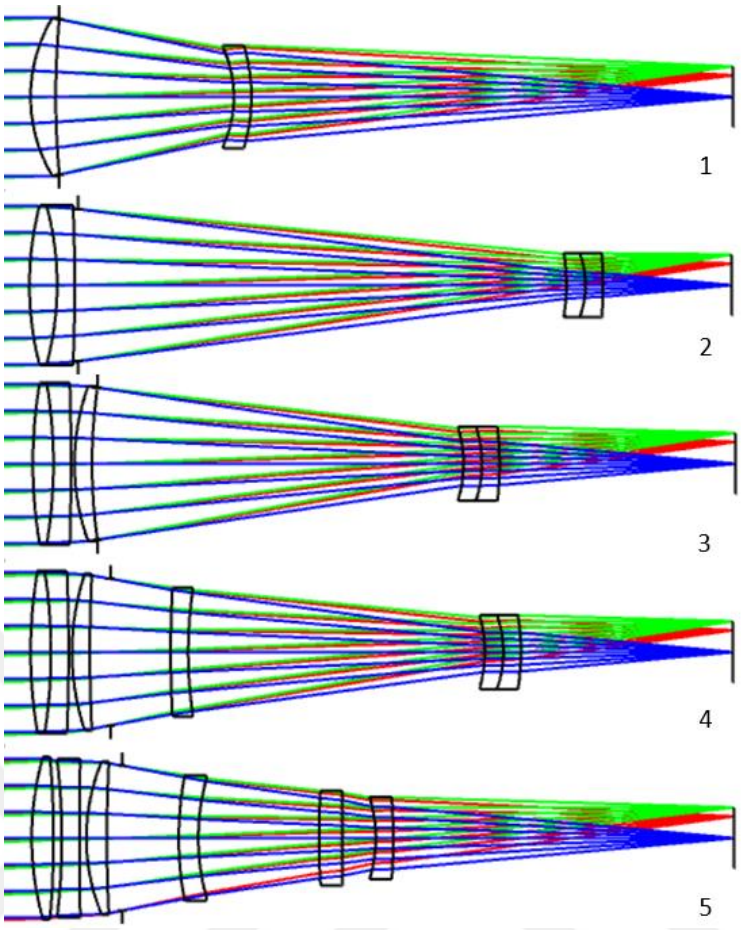

Figure 3.14 The design layout with five stages: (1) starting point with one positive and one negative lenses, (2) two lenses are converted into two cemented doublets, (3) additional lens are added in front of the stop, (4) additional lens are added behind the stop, (5) the air thickness between the lenses is introduced into the optical design.

Schott glass library was used for the optimization during the aforementioned stages in OpticStudio. For optimization, it is crucial to choose glass materials that can endure the harsh space environment when building optical systems for use in space [46]. The system then goes through optimization stages after ensuring sure the selected materials are suitable for the space environment. Rad-Hard is a library from OpticStudio that includes elements suitable for space. Materials with codes like BK7G18, F2G12, K5G20, LAK9G15, LF5G15, SF6G05, and SF8G07 can be found in this Rad-Hard library. The physical properties of these materials are presented in Table 3.3 [47]. High refractive indices and radiation resistance are two characteristics of these materials. Cerium is doped into these materials to increase radiation resistance, which might modify the substance's color [48]. The abbreviation in Table 3.3, n_d, V_d, ρ, T_g, Λ, and

$\alpha_{-30/+70}$ represents refractive index, abbe value, density, transformation temperature, thermal conductivity, and the coefficient of thermal expansion in the temperature range between – 30°C und + 70°C respectively.

Table 3.3 Physical properties of Rad-Hard library.

Material	n_d	V_d	ρ [g/cm^3]	T_g [°C]	Λ [W/(m*K)]	$\alpha_{-30/+70}$ [10^{-6}/K]
BK7G18	1.519	63.58	2.52	585	1.19	7.0
F2G12	1.621	36.56	3.60	435	0.82	8.1
K5G20	1.523	56.76	2.59	483	1	9.0
LAK9G15	1.691	54.76	3.53	634	0.88	6.3
LF5G15	1.584	40.83	3.22	407	0.86	9.3
SF6G05	1.809	25.28	5.20	427	-	7.8

The Rad-Hard materials are then used to re-optimize the optical system design. The optical design's components are gradually altered until only space-compatible materials are used to create the final optical design. This final design shows the Lens Data Editor (LDE) information in Table 3.4. The constrain parameters of this final optical design added to the Merit Function Editor are available in APPENDIX A.

Table 3.4 LDE of the final optical design.

Surface	**Comment**	**Radius**	**Thickness**	**Material**	**Diameter**
1	L1	161.446	15.980	K5G20	46.749
2		-214.195	4.412		46.246
3	L2	-195.245	9.996	SF6G05	44.850
4		303.998	3.996		43.696
5	L3	129.996	11.352	K5G20	43.720
6		4319.235	18.513		43.245
STOP		Infinity	32.489		40.011
8	L4	3235.632	9.996	LAK9G15	36.825
9		105.468	5.715		35.832
10	L5	130.657	10.173	SF6G05	36.541
11		-685.925	118.375		36.335
12	L6	-88.244	9.997	SF6G05	20.062
13		-226.881	149.007		20.396
14	Image Plane	Infinity	-	-	17.505

Figure 3.15, Figure 3.16, Figure 3.17, and Figure 3.18, respectively, show the layout, MTF, field curvature & distortion, and spot diagram of this final design.

The MTF value corresponding to the Nyquist frequency is seen in Figure 3.16 and Table 3.5. The high refractive index of lenses in the space-compatible glass catalog given in Table 3.3, the obstacles in making cemented doublets, and the high number of elements using spherical surfaces are the reasons for the decline in the MTF graph. As shown in Figure 3.17, the maximum distortion value is 0.12% for the maximum field. Field curvature sagittal and tangential values are 0.0028 mm, and 0.0793 mm, respectively. As shown in Figure 3.18, the Airy radius value is 3.981 µm. RMS radius and geometric radius values corresponding to angle values are given in Table 3.6.

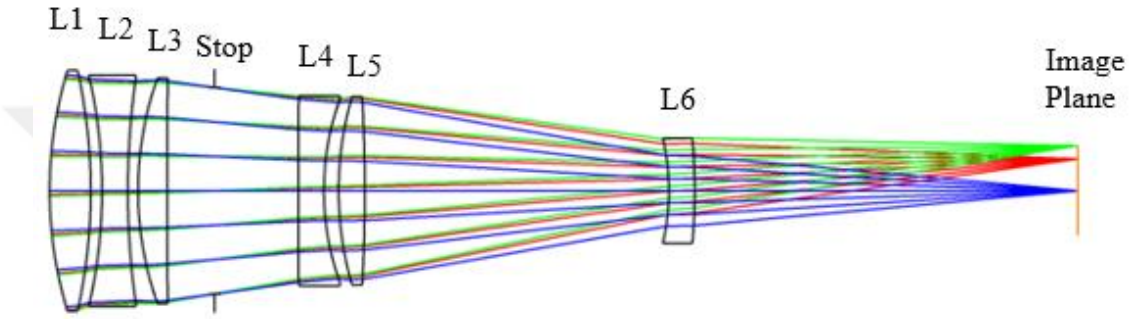

Figure 3.15 The design layout with compatible material for the space environment.

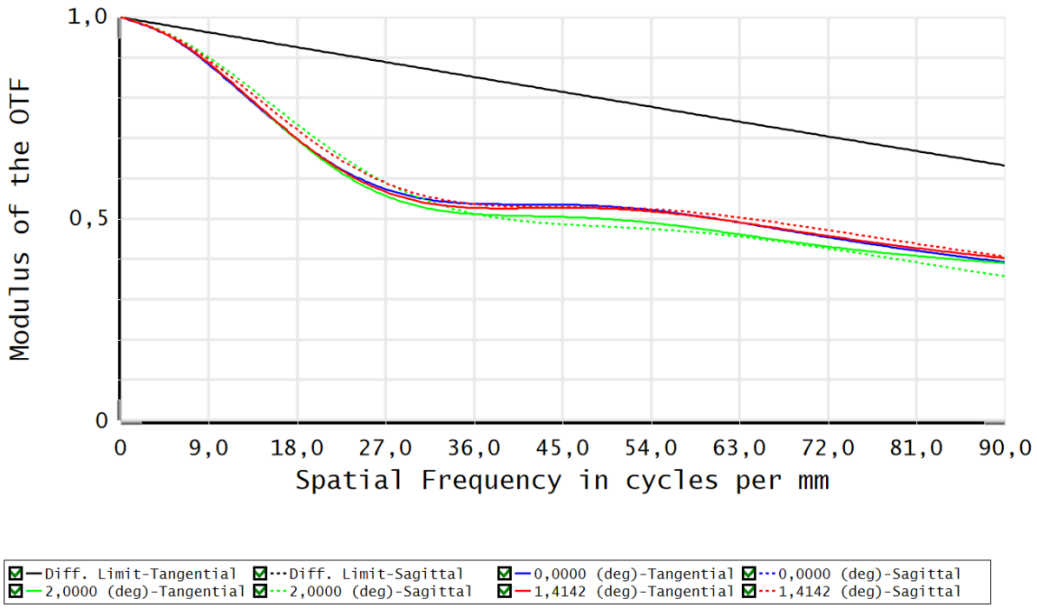

Figure 3.16 MTF curve at 90 lp/mm using the materials suitable for the space environment.

Table 3.5 MTF result of the final design at Nyquist frequency.

Field	Tangential (%)	Sagittal (%)
0º	39.2	39.2
1.4º	40.2	40.6
2.0º	38.9	35.7

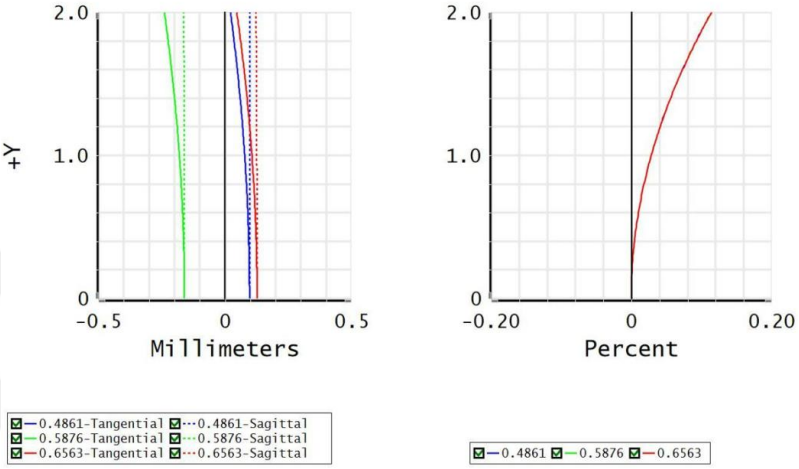

Figure 3.17 The diagram of the field curvature aberration and the distortion.

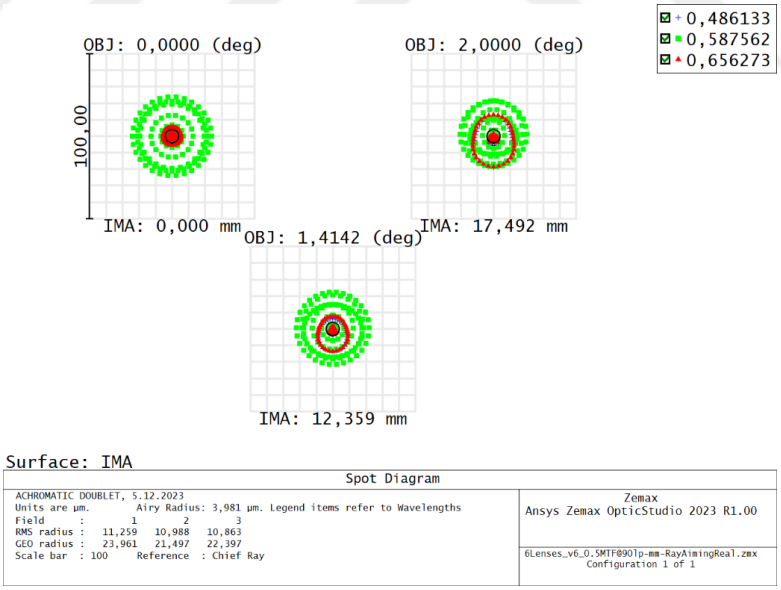

Figure 3.18 RMS spot diagram of the optical design.

Table 3.6 Spot diagram output.

Parameter	Unit	Field 1 (0º)	Field 2 (1.4º)	Field 3 (2.0º)
RMS Radius	µm	11.259	10.863	10.988
GEO Radius	µm	23.961	22.397	21.497
Airy Disk	µm	3.981	3.981	3.981

Full Field Display (FFD) of the third-order astigmatism, coma, and spherical aberrations of the final design are presented in Figure 3.19, Figure 3.20, and Figure 3.21, respectively. The FFDs show the distribution and amplitude of the aberrations through the fields.

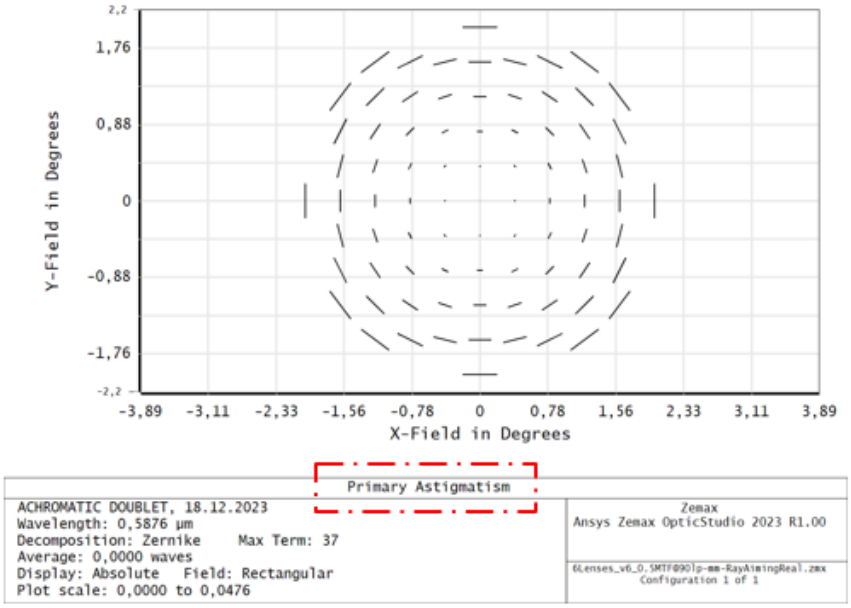

Figure 3.19 Full Field Display for the third-order astigmatism.

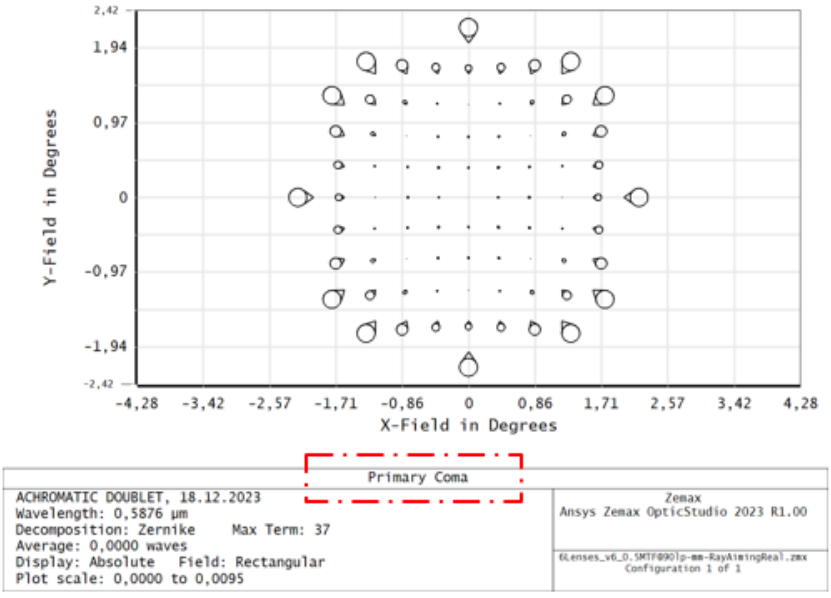

Figure 3.20 Full Field Display for the third-order coma.

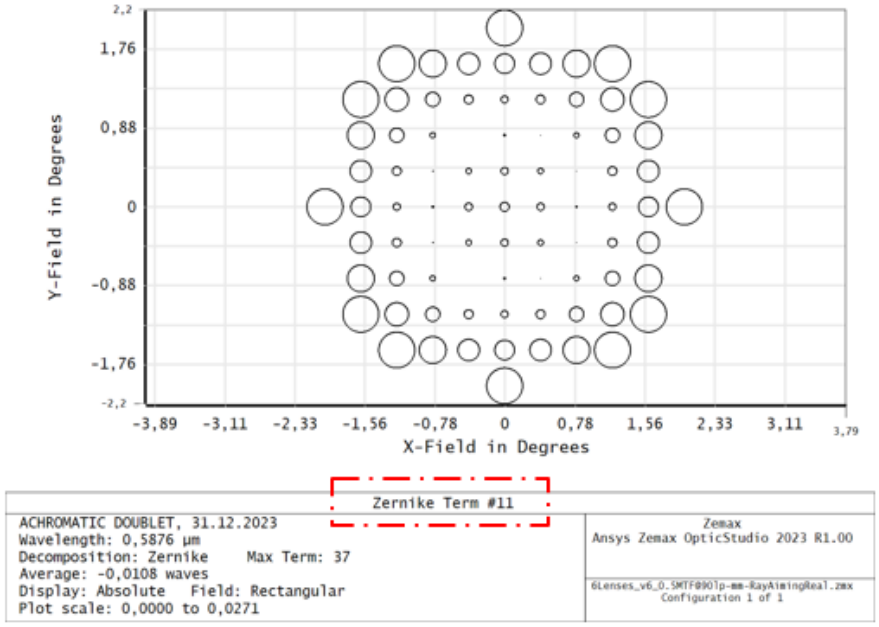

Figure 3.21 Full Field Display for the third-order spherical aberration.

3.6 Tolerance Analysis

Tolerance is a key competency for an optical engineer since it is essential to ensure that an optical system achieves its performance requirements. A methodology of OpticStudio's tolerance analysis is given in this section. The method takes manufacturing errors such as radius of curvature, thickness, surface irregularity (or surface from error), and misalignments such as tilt-decenter of the lenses into account. These values used in the analysis process are given in Table 3.7. During this analysis process, the mnemonic terms used in the tolerance data editor (TDE) for the parameters given in Table 3.7 are available in APPENDIX B.

Table 3.7 Tolerancing limits.

Parameter	Limit
Center thickness	±0.02 mm
Radius	±0.025% or 1 fringe
Element Tilt	±0.05 mm
Element Decenter	±0.05 mm
Surface Tilt	±0.004º
Surface Decenter	±0.01 mm
Lens Form Error	8 nm RMS

3.6.1 Sensitivity Analysis

Regarding tilt and decenter data, the effects of various components on optical system performance are thoroughly examined. The optical elements are subjected to sensitivity analysis, revealing details of each optical element's sensitivity in the system. Sensitivity analysis is carried out by considering two surfaces of each element in the optical system as a single element. Each optical system component is meticulously inspected for decenter values (TED) ranging from 10 to 50 µm and tilt values (TET) within the range of 10 to 50 milli-degrees. The findings are represented in Figure 3.22.

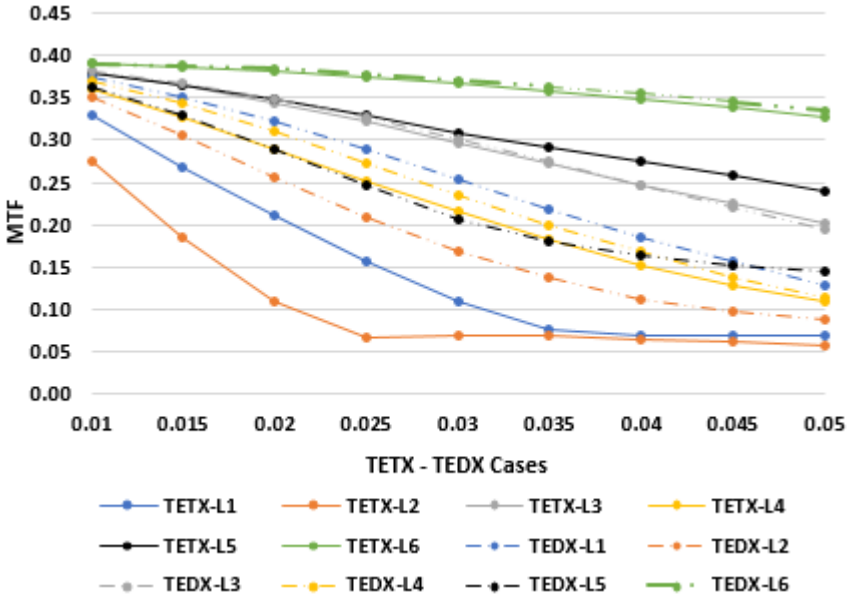

Figure 3.22 MTF graphs at Nyquist frequency for the sensitivity analysis.

Referring to Figure 3.22, an examination of the three most sensitive elements reveals that the lower orange line represents the tilt sensitivity of the 2nd optical element (L2), the second blue line represents the tilt sensitivity of the 1st optical element (L1), and the third line is illustrated the decentering sensitivity of the 2nd optical element. Based on the analysis results, it can be concluded that the system exhibited the tilt sensitivity as L2 > L1 > L4 > L3 > L5 > L6.

The system-level analysis follows individual analysis to keep the optical's mean MTF above 0.2 value. The system's constraints are based on the tilt value since the tilt parameter has the most impact on the system's sensitivity. The optical system analysis looks at the tilt range of 0 to 15 milli-degrees and the decenter range of 0 to 50 µm. The system's impact on tilt and decenter values is carefully evaluated. Figure 3.23 displays the Monte Carlo (MC) analysis outcomes with 500 trials at these intervals.

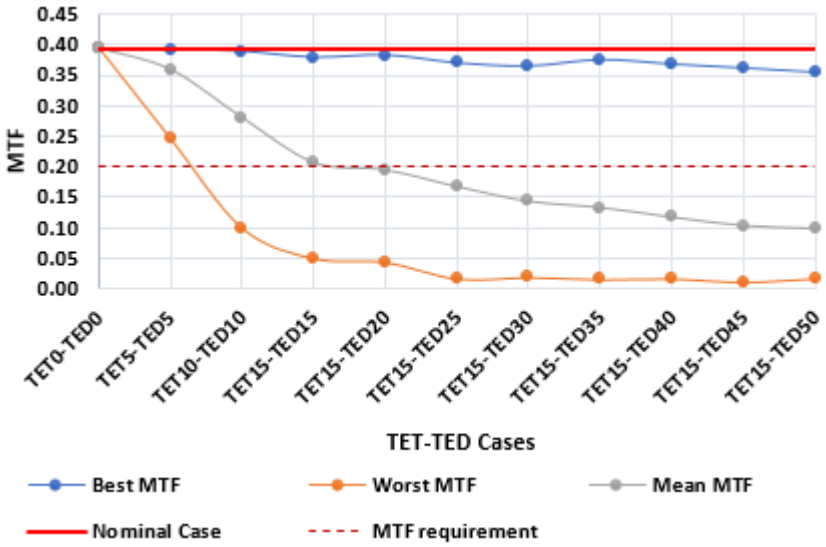

Figure 3.23 TET and TED & MTF @500 trial MC.

These findings conclude that the appropriate tilt value range for the system is 0–15 µm, while the acceptable decenter value range is 0–20 milli-degrees. In addition to the previously obtained tilt and decenter values, the optical elements' manufacturing capabilities are considered to enhance the study further. The OPTIMAX is used to create the optical manufacturing data [49]. Figure 3.24 shows the analysis's findings, which show how these TET and TED values affect the overall system including manufacturing effects.

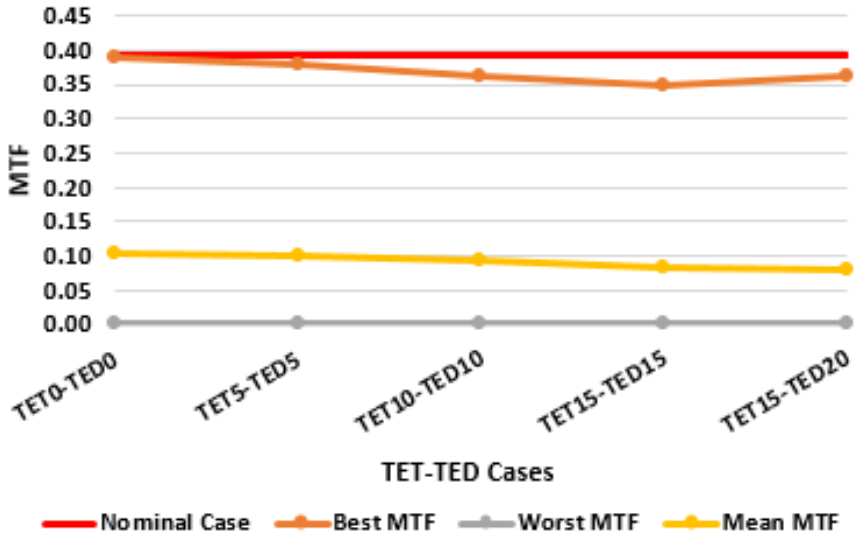

Figure 3.24 Tolerance analysis results of the objective without compensator.

3.6.2 Tolerance Analysis with Compensator

The most sensitive elements, determined by sensitivity analysis, are selected as compensators. A compensator is needed in the optical system since the mean MTF value with manufacturing does not achieve 0.2. The compensator is applied to the image plane in the TDE. The limit values added to the TDE are given in Table 3.8 (Surface-based decenter and tilt values are applied as 0.01 mm and 0.004^{o} on all optical element surfaces). The COMP command is introduced to the TDE as a compensating element and stands for the compensator. Giving the image plane a margin of around ±10 mm allows for the analysis. This image plane effect can be used as a natural compensation of the system when aligning. The analysis's findings are shown in Figure 3.25. RoC_1, RoC_2, t, and TEZI represent the radius of curvature of the optical element's first surface, the radius of curvature of the optical element's second surface, the center thickness of the optical element, and surface irregularity as shown in Table 3.8. The #, Nom, and Lim refer to number of lenses, the nominal value of the element, and the limit value of the element.

Table 3.8 Tolerance effect on the element of optical design with compensator.

#	Case	RoC_1	RoC_2	t [mm]	Δ TEDX [mm]	Δ TEDY [mm]	Δ TETX [mm]	Δ TETY [mm]	TEZI [nm]
L1	Nom	161.446	-214.195	15.98	0	0	0	0	7.9
	Lim	±0.04	±0.053	±0.02	±0.02	±0.02	±0.015	±0.015	7.9
L2	Nom	-195.245	303.998	9.996	0	0	0	0	7.9
	Lim	±0.049	±0.076	±0.02	±0.02	±0.02	±0.015	±0.015	7.9
L3	Nom	129.996	4319.235	11.352	0	0	0	0	7.9
	Lim	±0.033	±1.08	±0.02	±0.02	±0.02	±0.015	±0.015	7.9
L4	Nom	3235.632	105.468	9.996	0	0	0	0	7.9
	Lim	±0.809	±0.026	±0.02	±0.02	±0.02	±0.015	±0.015	7.9
L5	Nom	130.657	-685.925	10.173	0	0	0	0	7.9
	Lim	±0.033	±0.171	±0.02	±0.02	±0.02	±0.015	±0.015	7.9
L6	Nom	-88.244	-226.881	9.997	0	0	0	0	7.9
	Lim	±0.022	±0.057	±0.02	±0.02	±0.02	±0.015	±0.015	7.9

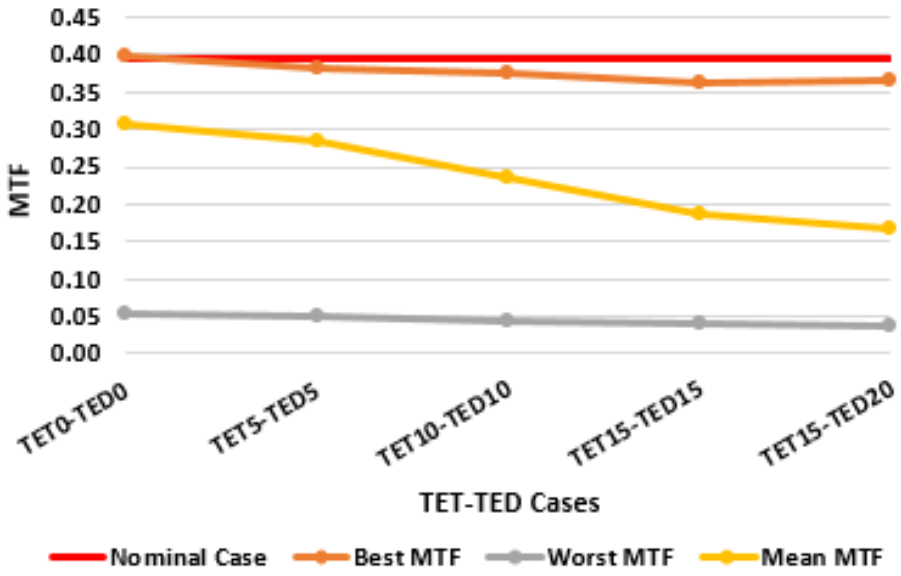

Figure 3.25 The data of ±10 mm image plane compensator.

These findings clearly show that the optical system's performance is still insufficient. It is decided that adding another compensator will improve this performance. As shown in Figure 3.26, the first triple lens group, which includes the most sensitive optical element, is regarded as a whole, and assigned the role of the second compensator of the system. The system design is set up for analysis, and during the study, new commands - CPAR are added to the commands. The results of that analysis are shown in Figure 3.27. The constrain parameters of this final optical design added to the TDE are available in APPENDIX C.

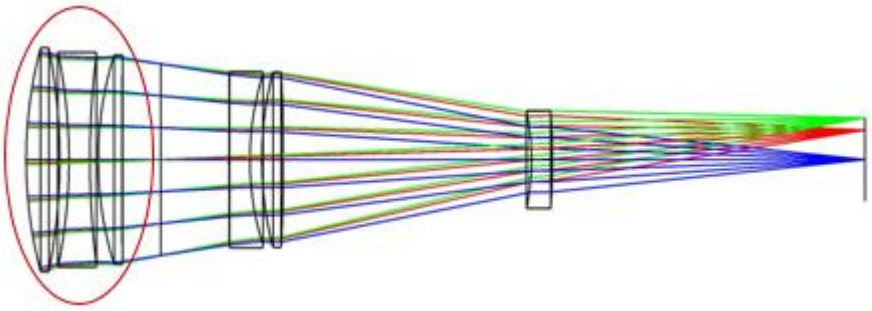

Figure 3.26 Defining the first triple lens group with a second compensator.

Figure 3.27 TET-TED cases with the image plane and the first group compensators.

The analysis results indicate that if the optical and optomechanical components are made within these manufacturing tolerances, the goal means MTF value in the electro-optical system may be attained at a minimum of 20%.

CHAPTER IV

MTF ANALYSIS

Modulation Transfer Function (MTF) analysis covers the factors that impact the overall MTF, such as optical manufacturing, alignment errors, and detector degradation effect as shown in Table 4.1. The MTF value of the final optical design is 35%. The effects of optical manufacturing and alignment error parameters in telescope realization are considered. As a result of the analysis, the telescope realization value is realized as 20%. The detector degradation effect is also taken as 58%.

Table 4.1 MTF Calculation on the electro-optic system.

Parameter	**MTF Value**
Optical Design	0.35
Telescope Realization (Optical Manufacturing, Alignment Errors)	0.20
Detector	0.58
Overall	**0.11**

The electro-optic camera's MTF value is calculated to be 11% when the effects of optical manufacturing, alignment errors, and detector degradation for the electro-optic system are considered. The effects of the satellite operation, which attenuates the electro-optic camera MTF performance, are listed in Table 4.2. The atmosphere effect is calculated as an attenuation of 0.02 [33]. It is budgeted that there will be a factor of 0.3 attenuation by the satellite.

Table 4.2 MTF calculation on the system.

Parameter	**Symbol**	**Value**
Atmosphere	$MTF_{atmosphere}$	0.98
Optics (with telescope realization)	MTF_{optics}	0.20
Detector	$MTF_{detector}$	0.58
Satellite	$MTF_{satellite}$	0.70
System *MTF*	MTF_{system}	**0.08**

The system MTF value is calculated to be 8% using Equation 2.9 which is an acceptable performance metric for the Earth observation.

CHAPTER V

SIGNAL-TO-NOISE RATIO

Satellite images must satisfy specific requirements, and these standards dictate the performance characteristics of the satellite. The signal-to-noise ratio (SNR), which measures the radiometric performance of the captured image and is computed for the light path from the Sun to the imager, is one important performance evaluation parameter for space-borne electro-optic imagers. SNR is the ratio of the imaging signal (S_{total}) to the total noise (σ_{total}) as given in the equation below [50].

$$SNR = \frac{S_{total}}{\sigma_{total}} \tag{5.1}$$

5.1 Calculation of the System Parameters

The parameters are calculated to be used in the SNR calculation. In this subsection, exposure time calculation, radiance calculation, calculation of the effects of telescope parameters, and calculation of the sensor parameters are performed, respectively.

5.1.1 The Exposure Time

The imager's exposure time is specified. As the amount of time needed to sweep the GSD across the Earth. The exposure time must be determined when the optical system observes the Earth from space. Some parameters must be calculated to determine the exposure time. Some of these variables are orbital and ground velocities, as shown in Figure 5.1.

Orbital velocity: The speed of the satellite needs to travel to maintain a stable orbit around a celestial body, such as the Earth.

Ground velocity: An object's horizontal motion about the surface of the Earth. It refers to the velocity at which an object travels over the surface of the Earth or along the ground.

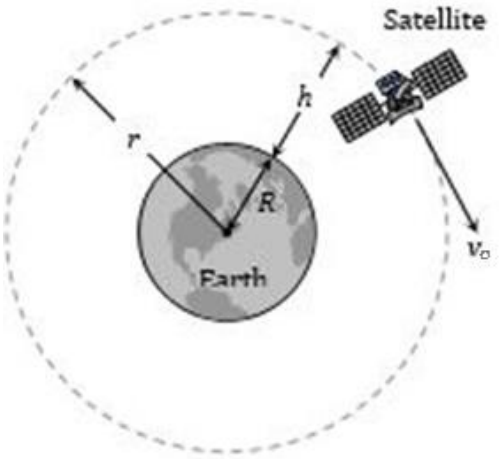

Figure 5.1 Schematic description of the orbital velocity and the ground velocity.

For calculating the sample time, both parameters are calculated, and the results are shown in Table 5.1, where *G*, *M*, and *R* stand for the gravitational constant, which is equal to 6.674 x 10^{-11} N-m^2/kg^2, Earth's mass, which is equal to 5.972 x 10^{24} kg, and Earth's radius, which is equal to 6.378 km, respectively.

Table 5.1 Calculation of the exposure time based on system parameters.

Parameter	Symbol	Function	Value
Orbital Velocity	v_0	$\sqrt{\frac{GM}{(R+h)}}$	7.67 km/s
Ground velocity	v_g	$\frac{R}{(R+h)} v_0$	7.22 km/s
Exposure Time	t_s	$\frac{GSD}{v_g}$	0.61 ms

5.1.2 Radiance

Sunlight rays can either be reflected or scattered from the Earth's surface as they reach the surface. Radiance gathered from the atmosphere is necessary to determine the signal value needed for the SNR calculation. This information is based on an end-to-end image chain encompassing radiance, telescope, sensor, and image components, as depicted in Figure 5.2. The radiance value is calculated using MODTRAN**,** a popular computer software for estimating radiance and atmospheric transmittance. The PcModWin/MODTRAN module is used in this section to get the atmospheric radiance data.

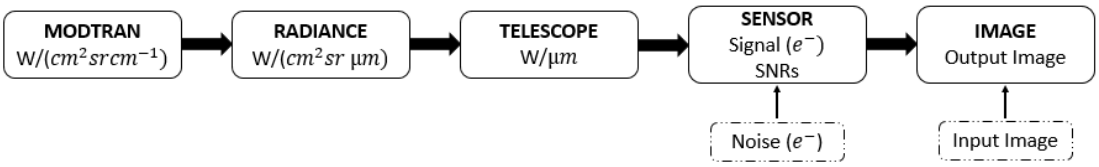

Figure 5.2 The SNR calculation's schematic image chain.

Figure 5.3 shows the outcomes of the spectral radiance calculated using MODTRAN. The Sun-Zenith angle (SZA) of 45° and a surface albedo of 0.15 are used to compute this spectral radiance. The Sun-Zenith angle is the angle between the surface normal and the incident sunlight, whereas surface albedo is the percentage of solar energy reflected by the Earth's surface. Within MODTRAN, the input parameters for a mission are specified. Table 5.2 provides more information used for the computation.

Table 5.2 MODTRAN input parameters.

Module	Parameter	Value
Geometry	Observer height	400 km
	Sun zenith angle	45°
	Nadir view	180°
	Wavelength bandwidth	400-700 km
	Atmosphere model	Mid-Latitude Summer
	Source	Sun
Atmosphere	Type of atmospheric path	Slant path to space of ground
	Mode of execution	Radiance with scattering
	CO2 mixing ratio	415 ppm
	Surface albedo, R(λ)	0.15
Aerosol	Aerosol model	Rural-VIS: 23 km
	Seasonal modifications to aerosol	Spring-Summer

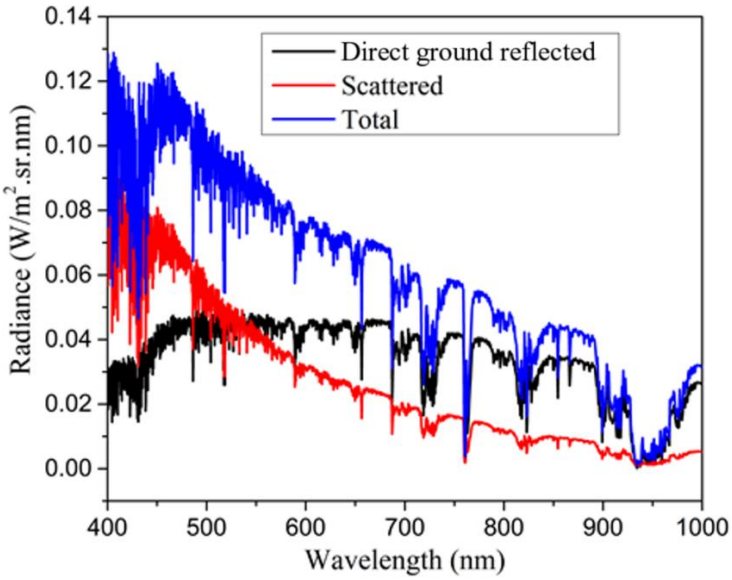

Figure 5.3 The spectral radiance, L(λ), obtained at 45° SZA and 0.15 albedo using MODTRAN [51].

5.2 Calculation of the SNR

The total signal generated by the sensor is calculated using the equation below.

$$S_{total} = L(\lambda) * \Omega * A * d\lambda * \tau_T(\lambda) * QE(\lambda) * t_s \quad [\bar{e}] \tag{5.2}$$

where, $L(\lambda), \Omega, A, d\lambda, \tau_T, QE(\lambda), t_s$ represents spectral radiance obtained from MODTRAN, solid angle, clear aperture area, spectral sampling distance, optic transmittance, spectral quantum efficiency, and exposure time, respectively.

Quantization noise (σ_{quan}), dark current (σ_{dark}), $1/f$ noise, and reset noise are just a few examples of the various components that make up the readout noise. Readout noise is frequently supplied by the sensor manufacturer. Shot noise (σ_{shot}) which is defined as a fluctuation in photocurrent and is brought by the nature of photons. Shot noise is the most prevalent type of noise for high-performance sensors, which limits the sensor performance. The shot noise is described as

$$\sigma_{shot} = \sqrt{S_{total}}[\bar{e}] \tag{5.3}$$

Total noise (σ_{total}) is calculated using the root sum squared (RSS) principle and defined by the following equation [50].

$$\sigma_{total} = \sqrt{\sigma_{shot}^2 + \sigma_{dark}^2 + \sigma_{quan}^2 + \cdots + \sigma_i^2}[\bar{e}] \tag{5.4}$$

where, the σ_i stands for individual noise sources.

SNR calculations are performed for the designed electro-optic imager. Table 5.3 represents the parameters used for the computations.

Table 5.3 The calculated parameters and system input of the electro-optic system.

Computation	**Parameters**	***Symbol***	**Value**
Satellite	Altitude	h	400 km
	Orbital velocity	v_0	7.67 km/s
	Ground velocity	v_g	7.22 km/s
	Exposure time	t_s	0.61 ms
Optical Design	Aperture	D	90 mm
	Effective focal length	f	500 mm
	Obscuration	τ_s	-
	Optical transmittance	τ_T	51%
	Reference wavelength	λ_{ref}	650 nm
	Ground sampling distance	GSD	4.4 m
	F-number	$f/\#$	5.5
	Q value ($(\lambda\ f/\#)/p$)	Q	0.65
Imaging Sensor	Pixel size	p	5.5 µm
	Pixel area	A_s	30.25 μm^2
	Pixel fill factor	FF	1
	Quantum efficiency	QE	50% (@555 nm)
	Spectral bandwidth	λ_{BW}	300-1100 nm
	Filter transmittance	τ_F	~ 94%
	Readout noise	σ_{read}	13 ē
	Dark current	I_λ	70 ē /s
	Quantization	N_{bits}	10 bits

In addition to the information in Table 5.3, when calculating optical transmittance, τ_T, the number of surfaces and materials the beam hits on its path is taken as a reference. It is calculated using the equation below.

$$\tau_T = \tau_{SF6G05}^4 * \tau_{K5G20}^6 * \tau_{LAK9G15}^2 \quad (5.5)$$

where τ_{K5G20}, τ_{SF6G05}, τ_{LAK9G15} represents optical transmittance value of K5G20, optical transmittance value of SF6G05, optical transmittance value of LAK9G15, respectively. The optical transmittance is calculated to be 51%.

Equation 5.1 and the code from the reference paper [51] are used to calculate SNR. The SNR is calculated to be 75 according to the given parameters.

CHAPTER VI

SUMMARY AND CONCLUSION

'*I have no idols, I admire work, dedication, and competence.*'

Ayrton Senna

Professors Jordi Puig-Suari of California Polytechnic State University and Bob Twiggs of Stanford University came up with the idea for CubeSats, which are miniature satellites that are primarily used in Low Earth Orbit (LEO) for a variety of purposes, such as atmospheric research, biological investigations, and climate assessments. These satellites adhere to standard dimensions while operating under defined parameters. It is clear from studying the CubeSat industry that optical systems frequently reflect optical designs. But as a piece of our research, we're looking into telephoto optical system designs, a subset of refractive systems. Earth observation is the normal use of these telephoto optical systems. This study intends to create a telephoto optical system design tailored for the CubeSat construction.

Before constructing the intended telephoto optical design, the satellite's critical system parameters are thoroughly established. These characteristics, including effective focal length, full field of view, swath width, F-number, aperture, and system MTF parameters, served as the basis for necessary system-level calculations. The goal is to match these estimates with the telephoto optical system design. A telephoto optical system, a subset of refractive systems, is chosen because of its distinctive advantages, particularly no obscuration. Additional advantages of this telephoto optical system design concept included meeting demanding higher field of view specifications while keeping a shorter system than the effective focal length. Several analysis are performed to clarify the system's length requirements before starting the design process. After thorough analysis, it is decided that a telephoto optical system design specially made to fit inside the 6U dimensions is the optimal choice. The optical design process developed gradually within the OpticStudio application, aligning with the systematically derived design specifications after the system size was firmly

established. Following the guidelines for telephoto optical system design, the initial stage of the design process started with a two-lenses configuration. These two lenses are then combined to create two sets of doublet lenses. The number of lenses gradually increased to meet the demanding electro-optic camera's MTF requirements. This iterative technique eventually ended up in a diffraction-limited optical design with six spherical lenses built to resist the extreme conditions of space environments.

To maintain the performance parameters of an optical system within the set restrictions, tolerance analysis is crucial in defining both the mechanical and optical manufacturing limitations. We meticulously examined each component of the final optical design in this study as part of a sensitivity analysis. The construction of a sensitivity rank, the result of this analytical work, sheds light on the sensitivity of the optical elements inside the optical system design. The system's response to mechanical tolerances is then thoroughly examined, providing us to determine the mechanical tolerance levels required for efficient system operations. We have expanded the scope of our analysis to include factors other than mechanical ones, such as the effect of the optical design on potential manufacturing errors. The optical design is evaluated holistically in the context of the overall system. Our study has enabled us to describe the system as an image plane compensator within the context of system engineering (CHAPTER II) to achieve the specified electro-optic camera's MTF target. But it soon became clear that the system's performance was not up to going. To fix this, we repeatedly add a second compensator to the analysis, providing the analysis closer to the targeted MTF value.

The effect of Modulation Transfer Function (MTF) values on the MTF budget in the selected detector design has been thoroughly examined in CHAPTER IV. The calculation shows how detector effects and tolerances affect MTF values, offering information on how each component affects system performance.

An electro-optic imaging system's Signal-to-Noise Ratio (SNR) is a crucial performance factor. Higher values of SNR indicate greater imaging quality, which is a measure of the quality of the executed image. The computed SNR value and the factors that affect it, such as exposure time, radiance, telescope characteristics, and sensor features, are thoroughly discussed in CHAPTER V. We used the capabilities of the MODTRAN program to compute radiance, which is crucial in this context. This work includes the application's internal parameters and the underlying mathematical calculations generated as the basis for our evaluations.

In summary, in this thesis, the telephoto optical system design for a 6U-sized CubeSat structure has been completed. It has an effective focal length of 500 mm and an FFOV of 2.58°. Six lenses in the design are constructed with space-compatible materials. OpticStudio has been used to carry out comprehensive design, sensitivity, and tolerance assessments of this telephoto optical system design. It has been established that the overall electro-optic camera's MTF value is better than 0.1.

This study shows that telephoto optical design, as one of the refractive elements, offers a viable alternative to reflective elements (e.g., Maksutov-Cassegrain or Ritchey-Chrétien) for attaining higher FFOVs and designing without obscuration.

REFERENCES

[1] C. Kitts *et al.*, “The GeneSat-1 Microsatellite Mission : A Challenge in Small Satellite Design,” in *20th Annual AıAA/USU Conference on Small Satellites*, 2006, pp. 1–6.

[2] J. Puig-suari, C. Turner, and R. J. Twiggs, “CubeSat: The Development and Launch Support Infrastructure for Eighteen Different Satellite Customers on One Launch,” in *15th Annual/USU Conference on Small Satellites*, 2001, pp. 1–5.

[3] S. Rohan, S. K. Saju, S. Syam, and Shabna, “Design And Development of A CubeSat for Atmospheric Research Design And Development of A CubeSat for Atmospheric Research,” *REST J. Emerg. trends Model. Manuf.*, vol. 9, no. 2, pp. 0–8, 2023, doi: https://doi.org/10.46632/jemm/9/2/1.

[4] S. M. Tieze, L. C. Liddell, S. R. S. Maria, and S. Bhattacharya, “BioSentinel: A Biological CubeSat for Deep Space Exploration,” *Astrobiology*, vol. 20, no. 8, pp. 1–6, 2020, doi: 10.1089/ast.2019.2068.

[5] H. C. Polat, J. Virgili-llop, and M. Romano, “Survey , Statistical Analysis and Classifica- tion of Launched CubeSat Missions with Emphasis on the Attitude Control Method,” *J. Small Satell.*, vol. 5, no. 3, pp. 513–530, 2016.

[6] V. Mani Karthik, A. S. Cassado, V. Franzese, A. Cervone, and F. Topputo, “Systems Design of MARIO : Stand-alone 16U CubeSat from Earth to Mars Systems Design of MARIO : Stand-alone 16U CubeSat from Earth to Mars,” in *70th International Astronautical Congress*, 2019, no. IAC–19–B4.8.3.x50968, pp. 1–17.

[7] M. Tumarina *et al.*, “Design , fabrication and space suitability tests of wide field of view , ultra-compact , and high resolution telescope for space application,” *Opt. Express*, vol. 26, no. 3, pp. 2390–2399, 2018, doi: 10.1002/asna.201111576.

[8] E. Kulu, “Nanosats Database,” *Nanosats*, 2014. nanosats.eu/cubesat (accessed Sep. 17, 2023).

[9] TÜBİTAK UZAY, “IMECE Satellite.” https://uzay.tubitak.gov.tr/en/projeler/imece

[10] B. Kurnaz, “LANDSAT-8 VE SENTİNEL-2 UYDU GÖRÜNTÜLERİ KULLANILARAK ORMAN YANGIN ALANI TESPİTİ: MUĞLA ÖRNEĞİ,” Zonguldak Bülent Ecevit University, 2019.

[11] D. G. Pitts and R. N. Kleinstein, *Environmental Vision: Interactions of the Eye , Vision , and the Environment*, First. United States of America: Reed Publishing, 1993.

[12] Z. Szantoi and E. S. Agency, *Earth Observation for Biodiversity Monitoring: Review of the use of remotely-sensed data for monitoring biodiversity change and tracking progress towards the aichi biodiversity targets*, no. 72. Montréal, Canada.: Secretariat of the Convention on Biological Diversity, 2014.

[13] Berlin Space Technologies, “BST HRVI-6hd 2nd Generation.” https://www.berlin-space-tech.com/wp-content/uploads/2022/12/PRF-PR-21_v1.1.0_HRVI-2nd-gen.pdf (accessed Nov. 25, 2023).

[14] D. Aerospace, “CAIMAN IMAGER High-performance Camera for CubeSats,” *Dragonfly Aerospace*, 2023. https://dragonflyaerospace.com/products/caiman/ (accessed Oct. 10, 2023).

[15] S. G. Ungar, J. S. Pearlman, J. A. Mendenhall, and D. Reuter, “Overview of the Earth Observing One (EO-1) Mission,” *IEEE*, vol. 41, no. 6, pp. 1149–1159, 2003.

[16] D. Gao, Q. Fu, Z. Zhao, B. Zhao, L. Zhong, and J. Zhan, “Design of Polarized Infrared Athermal Telephoto Objective for Penetrating The Fog,” *Proc. SPIE*, vol. 9300, no. 93001W, pp. 1–8, 2014, doi: 10.1117/12.2072669.

[17] J. Dong, Y. Zhang, S. Chen, H. Chen, and P. Guo, “Optical design and athermalization analysis of infrared dual band refractive-diffractive telephoto objective,” *Proc. SPIE*, vol. 10250, no. 102500H, pp. 1–5, 2017, doi:

10.1117/12.2266733.

[18] D. Mu, J. Dong, C. Xu, and Q. Li, “Infrared dual-band telephoto design used in joint transform correlator,” *Proc. SPIE*, vol. 8557, no. 855715, pp. 1–6, 2012, doi: 10.1117/12.979924.

[19] C. Xu, J. Dong, S. Zhang, and W. Wang, “Infrared Telephoto Design Used in Joint Transform Correlator,” *Key Eng. Mater.*, vol. 552, no. 1662–9795, pp. 21–26, 2013, doi: 10.4028/www.scientific.net/KEM.552.21.

[20] J. Dong, D. Mu, and C. Xu, “Athermal Design of Infrared Telephoto Used in Joint Transform Correlator,” *Key Eng. Mater.*, vol. 552, no. 1662–9795, pp. 57–63, 2013, doi: 10.4028/www.scientific.net/KEM.552.57.

[21] M. Gardner, P. Rogers, M. Wilde, T. Cook, and A. Shipton, “Challenges and solutions for high performance SWIR lens design,” *Proc. SPIE*, vol. 9987, no. 99870C, pp. 1–16, 2016, doi: 10.1117/12.2241089.

[22] A. E. Şahin, “Görünür ve Kızılötesi Uygulamalar İçim Mercek Grubunun Tasarımı,” GAZİ UNIVERSITY, 2020.

[23] Z. Yu, S. Ji-yang, XuYue, and W. Wen-sheng, “Design of cooled Athermalized Infrared Telephoto Lens,” *Proc. SPIE*, vol. 8557, no. 855716, pp. 2–9, 2012, doi: 10.1117/12.999327.

[24] OSRAM, “OSRAM AMS CMV12000 Datasheet,” *ams OSRAM Group*, 2022. https://ams.com/documents/20143/36005/CMV12000_DS000603_5-00.pdf (accessed Apr. 10, 2023).

[25] TELEDYNE, “Field of View and Angular Field of View Educational Notes,” *Teledeyne Princeton Instruments*, 2023. https://www.princetoninstruments.com/learn/camera-fundamentals/field-of-view-and-angular-field-of-view (accessed Jul. 27, 2023).

[26] B. Waterman, “Investigating Ions ’ Effects on the Fluorescent Protein Dendra2,” The University of Maine, 2019.

[27] I. S. Volume, “Airy Disk.” svi.nl/AiryDisk (accessed Dec. 20, 2023).

[28] T. B. BELDEK, “Short Wave Infrared Camera Design and Focal Plane Analysis,” Middle East Technical University, 2012.

[29] Edmund Optics, “Introduction to Modulation Transfer Function.”

[30] N. A. A. Galaom, “Integration of a MEMS-based Autofocus Actuator into a Smartphone Camera,” University of Toronto, 2016.

[31] W. J. Smith, *Modern Optical Engineering*, Fourth Edi. Carlsbad, California: The McGraw-Hill, 2008. doi: 10.1036/0071476873.

[32] DxOMark Labs Company, “Modulation Transfer Function (MTF).” http://www.dxomark.com/About/In-depth-measurements/Measurements/Sharpness. (accessed Dec. 19, 2023).

[33] Z. N. Öztürk, E. Ceylan, C. Deniz, M. Ekinci, M. B. Ekinci, and Ö. Karcı, “End-to-End Modulation Transfer Function (MTF) Simulator for High-Resolution Spaceborne Electro- Optic Imagers,” *2023 10th Int. Conf. Recent Adv. Air Sp. Technol. (RAST), İstanbul, Turkiye*, pp. 1–7, 2023, doi: 10.1109/RAST57548.2023.10197886.

[34] K. B. Alici, O. Selimoglu, O. Karci, A. S. Yılmaz, C. Özdemir, and F. S. Okten, “OTF Analysis of a Spaceborne CMOS Imaging Sensor,” *IEEE*, no. November 2018, pp. 133–138, 2017, doi: 10.1109/RAST.2017.8002972.

[35] H. Gross, F. Blechinger, and B. Achtner, *Handbook of Optical Systems*, Vol. 4 Sur., vol. 4. Weinheim, Germany: Copyright © 2008 WILEY-VCH Verlag GmbH & Co. KGaA, 2008.

[36] D. Malacara and Z. Malacara, *Handbook of Optical Design*, Second. Madison Avenue, New York, NY 10016: Copyright _ 2004 by Marcel Dekker, Inc. All Rights Reserved, 2004.

[37] C. Olson and J. Bentley, *Field Guide to Lens Design*, First. Bellingham, Washington, USA: 012 Society of Photo-Optical Instrumentation Engineers (SPIE), 2012.

[38] J. R. B. Kingslake Rudolf, *Lens Design Fundamentals*, Second. Bellingham, Washington, USA: SPIE Press, 2010.

[39] Y. Zheng, S. Lin, C. Kambhamettu, J. Yu, S. B. Kang, and S. Member, "Single-Image Vignetting Correction," *IEEE Trans. Pattern Anal. Mach. Intell.*, vol. 31, no. 12, pp. 2243–2256, 2009, doi: 10.1109/TPAMI.2008.263.

[40] F. L. Pedrotti, L. M. Pedrotti, and L. S. Pedrotti, *Introduction to Optics*, Third Edit.

[41] K. Thompson, "Description of the third-order optical aberrations of near-circular pupil optical systems without symmetry," *Opt. Soc. Am.*, vol. 22, no. 7, pp. 1389–1401, 2005.

[42] K. P. Thompson, T. Schmid, and J. P. Rolland, "Recent Discoveries from Nodal Aberration Theory," *Opt. Soc. Am. Inc.*, 2010, doi: 10.1117/12.871018.

[43] R. Dimartino, "Designing Optical Systems for Space Projects," *Resolve Optics Ltd*, 2020. ien.eu/article/designing-optical-systems-for-space-projects-3/ (accessed Aug. 15, 2023).

[44] Z. Jiao, L. Jiang, J. Sun, J. Huang, and Y. Zhu, "Outgassing Environment of Spacecraft : An Overview Outgassing Environment of Spacecraft : An Overview," *IOP Conf. Ser. Mater. Sci. Eng.*, vol. 611, no. 012071, pp. 1–8, 2019, doi: 10.1088/1757-899X/611/1/012071.

[45] H. Pollicove and D. Golini, "Deterministic Manufacturing Processes for Precision Optical Surfaces," *Key Eng. Mater.*, vol. 2038, no. 2039, pp. 53–58, 2003, doi: 10.4028/www.scientific.net/KEM.238-239.53.

[46] S. Biryuchinskiy, S. Churayeu, and Y. Jeong, "Compact Optical Systems for Space Applications," *J. Sp. Technol. Appl.*, vol. 1, no. 1, pp. 104–120, 2021, doi: 10.52912/jsta.2021.1.1.104.

[47] Schott AG, "Optical Glass Data Sheets Inquiry Glass," Germany, 2019.

[48] M. Ghigo and P. Spano, "Space-qualified glass database," 2009. [Online]. Available: https://slideplayer.com/slide/6932813/

[49] Optimax, "Manufacturing Tolerance Chart," *Optimax Knowledge Center,*. https://www.optimaxsi.com/charts/manufacturing-tolerance-chart/ (accessed Sep. 11, 2022).

[50] G. C. Holst, *Ccd Arrays, Cameras and Displays*, Second. Bellingham, Washington USA: SPIE Press, 1998.

[51] Z. N. Öztürk, İ. Başlar, Ö. Selimoğlu, and Ö. Karcı, "Signal-to-noise ratio model in Python for high-resolution space-borne electro-optic imagers," *J. Remote Sens.*, vol. 17, no. 1, pp. 1–18, 2023, doi: 10.1117/1.JRS.17.014508.

APPENDIX A

MERIT FUNCTION EDITOR FOR FINAL OPTICAL DESIGN

	Type		Wave	Hx	Hy	Px	Py		Target	Weight	Value	% Contrib
1	EFFL		2						500,000	1,000	499,995	4,694E-03
2	BLNK											
3	MTFA	1	0	1	100,000	1	0		0,400	1,000	0,368	32,296
4	MTFA	1	0	2	100,000	1	0		0,400	1,000	0,341	36,500
5	MTFA	1	0	3	100,000	1	0		0,400	1,000	0,376	31,120
6	BLNK											
7	DMFS											
8	BLNK	Sequential merit function: RMS spot x+y centroid X Wgt = 1,0000 Y Wgt = 1,0000 GQ 5 rings										
9	BLNK	Default individual air and glass thickness boundary constraints.										
10	MNCA	1	1						4,000	1,000	4,000	0,000
11	MXCA	1	1						1000,000	1,000	1000,000	0,000
12	MNEA	1	1	0,000	0				4,000	1,000	4,000	0,000
13	MNCG	1	1						10,000	1,000	10,000	0,000
14	MXCG	1	1						25,000	1,000	25,000	0,000
15	MNEG	1	1	0,000	0				4,000	1,000	4,000	0,000
16	MNCA	2	2						4,000	1,000	4,000	0,000
17	MXCA	2	2						1000,000	1,000	1000,000	0,000
18	MNEA	2	2	0,000	0				4,000	1,000	4,000	0,000
19	MNCG	2	2						10,000	1,000	10,000	0,000
20	MXCG	2	2						25,000	1,000	25,000	0,000
21	MNEG	2	2	0,000	0				4,000	1,000	4,000	0,000
22	MNCA	3	3						4,000	1,000	4,000	0,000
23	MXCA	3	3						1000,000	1,000	1000,000	0,000
24	MNEA	3	3	0,000	0				4,000	1,000	4,000	0,000
25	MNCG	3	3						10,000	1,000	9,996	3,429E-03
26	MXCG	3	3						25,000	1,000	25,000	0,000
27	MNEG	3	3	0,000	0				4,000	1,000	4,000	0,000
28	MNCA	4	4						4,000	1,000	3,996	2,864E-03

Figure A.1 Merit Function Editor for the final optical design-1.

29	MXCA	4	4						1000,000	1,000	1000,000	0,000
30	MNEA	4	4	0,000	0				4,000	1,000	4,000	0,000
31	MNCG	4	4						10,000	1,000	10,000	0,000
32	MXCG	4	4						25,000	1,000	25,000	0,000
33	MNEG	4	4	0,000	0				4,000	1,000	4,000	0,000
34	MNCA	5	5						4,000	1,000	4,000	0,000
35	MXCA	5	5						1000,000	1,000	1000,000	0,000
36	MNEA	5	5	0,000	0				4,000	1,000	4,000	0,000
37	MNCG	5	5						10,000	1,000	10,000	0,000
38	MXCG	5	5						25,000	1,000	25,000	0,000
39	MNEG	5	5	0,000	0				4,000	1,000	3,996	2,591E-03
40	MNCA	6	6						4,000	1,000	4,000	0,000
41	MXCA	6	6						1000,000	1,000	1000,000	0,000
42	MNEA	6	6	0,000	0				4,000	1,000	4,000	0,000
43	MNCG	6	6						10,000	1,000	10,000	0,000
44	MXCG	6	6						25,000	1,000	25,000	0,000
45	MNEG	6	6	0,000	0				4,000	1,000	4,000	0,000
46	MNCA	7	7						4,000	1,000	4,000	0,000
47	MXCA	7	7						1000,000	1,000	1000,000	0,000
48	MNEA	7	7	0,000	0				4,000	1,000	4,000	0,000
49	MNCG	7	7						10,000	1,000	10,000	0,000
50	MXCG	7	7						25,000	1,000	25,000	0,000
51	MNEG	7	7	0,000	0				4,000	1,000	4,000	0,000
52	MNCA	8	8						4,000	1,000	4,000	0,000
53	MXCA	8	8						1000,000	1,000	1000,000	0,000
54	MNEA	8	8	0,000	0				4,000	1,000	4,000	0,000
55	MNCG	8	8						10,000	1,000	9,996	2,958E-03
56	MXCG	8	8						25,000	1,000	25,000	0,000

Figure A.2 Merit Function Editor for the final optical design-2.

57	MNEG	8	8	0,000	0				4,000	1,000	4,000	0,000
58	MNCA	9	9						4,000	1,000	4,000	0,000
59	MXCA	9	9						1000,000	1,000	1000,000	0,000
60	MNEA	9	9	0,000	0				4,000	1,000	4,000	0,000
61	MNCG	9	9						10,000	1,000	10,000	0,000
62	MXCG	9	9						25,000	1,000	25,000	0,000
63	MNEG	9	9	0,000	0				4,000	1,000	4,000	0,000
64	MNCA	10	10						4,000	1,000	4,000	0,000
65	MXCA	10	10						1000,000	1,000	1000,000	0,000
66	MNEA	10	10	0,000	0				4,000	1,000	4,000	0,000
67	MNCG	10	10						10,000	1,000	10,000	0,000
68	MXCG	10	10						25,000	1,000	25,000	0,000
69	MNEG	10	10	0,000	0				4,000	1,000	3,996	2,859E-03
70	MNCA	11	11						4,000	1,000	4,000	0,000
71	MXCA	11	11						1000,000	1,000	1000,000	0,000
72	MNEA	11	11	0,000	0				4,000	1,000	4,000	0,000
73	MNCG	11	11						10,000	1,000	10,000	0,000
74	MXCG	11	11						25,000	1,000	25,000	0,000
75	MNEG	11	11	0,000	0				4,000	1,000	4,000	0,000
76	MNCA	12	12						4,000	1,000	4,000	0,000
77	MXCA	12	12						1000,000	1,000	1000,000	0,000
78	MNEA	12	12	0,000	0				4,000	1,000	4,000	0,000
79	MNCG	12	12						10,000	1,000	9,997	1,367E-03
80	MXCG	12	12						25,000	1,000	25,000	0,000
81	MNEG	12	12	0,000	0				4,000	1,000	4,000	0,000
82	MNCA	13	13						4,000	1,000	4,000	0,000
83	MXCA	13	13						1000,000	1,000	1000,000	0,000
84	MNEA	13	13	0,000	0				4,000	1,000	4,000	0,000

Figure A.3 Merit Function Editor for the final optical design-3.

85	MNCG	13	13						10,000	1,000	10,000	0,000
86	MXCG	13	13						25,000	1,000	25,000	0,000
87	MNEG	13	13	0,000	0				4,000	1,000	4,000	0,000

Figure A.4 Merit Function Editor for the final optical design-4.

APPENDIX B

MNEMONIC TERMS OF THE TOLERANCE DATA EDITOR

Table B.1 Mnemonic terms of the Tolerance Data Editor

Mnemonic	Explanation
TRAD, TCUR, TFRN	Tolerance on radius
TTHI	Tolerance on thickness
TIRR	Tolerance on standard surface irregularity
TEZI	Tolerance on surface irregularity using Zernike standard polynomials
TEDX, TEDY	Tolerance on element decenters
TETX, TETY, TETZ	Tolerance on element tilts in degrees
TSDX, TSDY	Tolerance on surface decenters
TSTX, TSTY	Tolerance on surface tilt in degrees
TIRX, TIRY	Tolerance on total indicator runout in lens units
COMP	Sets a thickness, radius, or conic compensator
CPAR	Sets a parameter as a compensator
TIND	Tolerance on index
TPAR, TEDV	Tolerance on parameters, and extra data values
TUDX, TUDY	Tolerance on coordinate break decenters
TUTX, TUTY, TUTZ	Tolerance on coordinate break tilts
TCON	Tolerance on conic

APPENDIX C

TOLERANCE DATA EDITOR FOR FINAL OPTICAL DESIGN

	Type				Nominal			Comment
1	TWAV					0,633		Default test wavelength.
2	COMP	27	0		149,007	-10,000	10,000	Default compensator on back focus.
3	CPAR	1	1		0,000	-1,000	1,000	First Lens Group TEDx Comp.
4	CPAR	1	2		0,000	-1,000	1,000	First Lens Group TEDy Comp.
5	CPAR	1	3		0,000	-1,000	1,000	First Lens Group TETx Comp.
6	CPAR	1	4		0,000	-1,000	1,000	First Lens Group TETy Comp.
7	TOFF							-----
8	TOFF							L1:Left Surface
9	TTHI	2	2		15,980	-0,020	0,020	L1:Left Thickness (mm)
10	TRAD	2	0		161,446	-0,040	0,040	L1:Left Surface: Radius of Curvature (mm)
11	TEDX	2	4		0,000	-0,020	0,020	L1:Left Surface: X-Decenter,element (mm)
12	TEDY	2	4		0,000	-0,020	0,020	L1:Left Surface: Y-Decenter, element (mm)
13	TETY	2	4		0,000	-0,015	0,015	L1:Left Surface: Y-Tilt, element (degree)
14	TETX	2	4		0,000	-0,015	0,015	L1:Left Surface: X-Tilt, element (degree)
15	TEZI	2	37	5	0,000	-7,900E-06	7,900E-06	L1:Left Surface: Zernike RMS WFE (mm)
16	TSDX	2			0,000	-1,000E-02	1,000E-02	L1:Left Surface: X-Decenter, surface (mm)
17	TSDY	2			0,000	-1,000E-02	1,000E-02	L1:Left Surface: Y-Decenter, surface (mm)
18	TSTX	2			0,000	-4,000E-03	4,000E-03	L1:Left Surface: X-Tilt, surface (degree)
19	TSTY	2			0,000	-4,000E-03	4,000E-03	L1:Left Surface: Y-Tilt, surface (degree)
20	TOFF							L1:Left Surface End
21	TOFF							L1:Right Surface
22	TTHI	4	4		4,412	-0,020	0,020	L1:Right Air Thickness (mm)
23	TRAD	4	0		-214,195	-0,053	0,053	L1:Right Surface: Radius of Curvature (mm)
24	TEZI	4	37	5	0,000	-7,900E-06	7,900E-06	L1:Right Surface: Zernike RMS WFE (mm)
25	TSDX	4			0,000	-1,000E-02	1,000E-02	L1:Right Surface: X-Decenter, surface (mm)
26	TSDY	4			0,000	-1,000E-02	1,000E-02	L1:Right Surface: Y-Decenter, surface (mm)
27	TSTX	4			0,000	-4,000E-03	4,000E-03	L1:Right Surface: X-Tilt, surface (degree)
28	TSTY	4			0,000	-4,000E-03	4,000E-03	L1:Right Surface: Y-Tilt, surface (degree)

Figure C.1 Tolerance Data Editor for the final optical design-1.

29	TOFF							L1:Right Surface End
30	TOFF							First Surface End !!!
31	TOFF							-----
32	TOFF							>>>Second Lens: L2
33	TOFF							L2:Left Surface
34	TTHI	6	6		9,996	-0,020	0,020	L2:Left Thickness (mm)
35	TRAD	6	0		-195,245	-0,049	0,049	L2:Left Surface: Radius of Curvature (mm)
36	TEDX	6	8		0,000	-0,020	0,020	L2:Left Surface: X-Decenter, element (mm)
37	TEDY	6	8		0,000	-0,020	0,020	L2:Left Surface: Y-Decenter, element (mm)
38	TETY	6	8		0,000	-0,015	0,015	L2:Left Surface: Y-Tilt, element (degree)
39	TETX	6	8		0,000	-0,015	0,015	L2:Left Surface: X-Tilt, element (degree)
40	TEZI	6	37	5	0,000	-7,900E-06	7,900E-06	L2:Left Surface: Zernike RMS WFE (mm)
41	TSDX	6			0,000	-1,000E-02	1,000E-02	L2:Left Surface: X-Decenter, surface (mm)
42	TSDY	6			0,000	-1,000E-02	1,000E-02	L2:Left Surface: Y-Decenter, surface (mm)
43	TSTX	6			0,000	-4,000E-03	4,000E-03	L2:Left Surface: X-Tilt, surface (degree)
44	TSTY	6			0,000	-4,000E-03	4,000E-03	L2:Left Surface: Y-Tilt, surface (degree)
45	TOFF							L2:Left Surface End
46	TOFF							L2:Right Surface
47	TTHI	8	8		3,996	-0,020	0,020	L2:Right Air Thickness (mm)
48	TRAD	8	0		303,998	-0,076	0,076	L2:Right Surface: Radius of Curvature (mm)
49	TEZI	8	37	5	0,000	-7,900E-06	7,900E-06	L2:Right Surface: Zernike RMS WFE (mm)
50	TSDX	8			0,000	-1,000E-02	1,000E-02	L2:Right Surface: X-Decenter, surface (mm)
51	TSDY	8			0,000	-1,000E-02	1,000E-02	L2:Right Surface: Y-Decenter, surface (mm)
52	TSTX	8			0,000	-4,000E-03	4,000E-03	L2:Right Surface: X-Tilt, surface (degree)
53	TSTY	8			0,000	-4,000E-03	4,000E-03	L2:Right Surface: Y-Tilt, surface (degree)
54	TOFF							L2:Right Surface End
55	TOFF							Second Surface End !!!
56	TOFF							-----

Figure C.2 Tolerance Data Editor for the final optical design-2.

57	TOFF							>>>Third Lens: L3
58	TOFF							L3:Left Surface
59	TTHI	10	10		11,352	-0,020	0,020	L3:Left Thickness (mm)
60	TRAD	10	0		129,996	-0,033	0,033	L3:Left Surface: Radius of Curvature (mm)
61	TEDX	10	12		0,000	-0,020	0,020	L3:Left Surface: X-Decenter, element (mm)
62	TEDY	10	12		0,000	-0,020	0,020	L3:Left Surface: Y-Decenter, element (mm)
63	TETY	10	12		0,000	-0,015	0,015	L3:Left Surface: Y-Tilt, element (degree)
64	TETX	10	12		0,000	-0,015	0,015	L3:Left Surface: X-Tilt, element (degree)
65	TEZI	10	37	5	0,000	-7,900E-06	7,900E-06	L3:Left Surface: Zernike RMS WFE (mm)
66	TSDX	10			0,000	-1,000E-02	1,000E-02	L3:Left Surface: X-Decenter, surface (mm)
67	TSDY	10			0,000	-1,000E-02	1,000E-02	L3:Left Surface: Y-Decenter, surface (mm)
68	TSTX	10			0,000	-4,000E-03	4,000E-03	L3:Left Surface: X-Tilt, surface (degree)
69	TSTY	10			0,000	-4,000E-03	4,000E-03	L3:Left Surface: Y-Tilt, surface (degree)
70	TOFF							L3:Left Surface End
71	TOFF							L3:Right Surface
72	TTHI	14	14		18,513	-0,020	0,020	L3:Right Air Thickness (mm)
73	TRAD	12	0		4319,235	-1,080	1,080	L3:Right Surface: Radius of Curvature (mm)
74	TEZI	12	37	5	0,000	-7,900E-06	7,900E-06	L3:Right Surface: Zernike RMS WFE (mm)
75	TSDX	12			0,000	-1,000E-02	1,000E-02	L3:Right Surface: X-Decenter, surface (mm)
76	TSDY	12			0,000	-1,000E-02	1,000E-02	L3:Right Surface: Y-Decenter, surface (mm)
77	TSTX	12			0,000	-4,000E-03	4,000E-03	L3:Right Surface: X-Tilt, surface (degree)
78	TSTY	12			0,000	-4,000E-03	4,000E-03	L3:Right Surface: Y-Tilt, surface (degree)
79	TOFF							L3:Right Surface End
80	TOFF							Third Surface End !!!
81	TOFF							-----
82	TOFF							>>>STOP
83	TOFF							-----

Figure C.3 Tolerance Data Editor for the final optical design-3.

84	TOFF							>>>Fourth Lens: L4
85	TOFF							L4:Left Surface
86	TTHI	17	17		9,996	-0,020	0,020	L4:Left Thickness (mm)
87	TRAD	17	0		3235,632	-0,809	0,809	L4:Left Surface: Radius of Curvature (mm)
88	TEDX	17	19		0,000	-0,020	0,020	L4:Left Surface: X-Decenter, element (mm)
89	TEDY	17	19		0,000	-0,020	0,020	L4:Left Surface: Y-Decenter, element (mm)
90	TETY	17	19		0,000	-0,015	0,015	L4:Left Surface: Y-Tilt, element (degree)
91	TETX	17	19		0,000	-0,015	0,015	L4:Left Surface: X-Tilt, element (degree)
92	TEZI	17	37	5	0,000	-7,900E-06	7,900E-06	L4:Left Surface: Zernike RMS WFE (mm)
93	TSDX	17			0,000	-1,000E-02	1,000E-02	L4:Left Surface: X-Decenter, surface (mm)
94	TSDY	17			0,000	-1,000E-02	1,000E-02	L4:Left Surface: Y-Decenter, surface (mm)
95	TSTX	17			0,000	-4,000E-03	4,000E-03	L4:Left Surface: X-Tilt, surface (degree)
96	TSTY	17			0,000	-4,000E-03	4,000E-03	L4:Left Surface: Y-Tilt, surface (degree)
97	TOFF							L4:Left Surface End
98	TOFF							L4:Right Surface
99	TTHI	19	19		5,715	-0,020	0,020	L4:Right Air Thickness (mm)
100	TRAD	19	0		105,468	-0,026	0,026	L4:Right Surface: Radius of Curvature (mm)
101	TEZI	19	37	5	0,000	-7,900E-06	7,900E-06	L4:Right Surface: Zernike RMS WFE (mm)
102	TSDX	19			0,000	-1,000E-02	1,000E-02	L4:Right Surface: X-Decenter, surface (mm)
103	TSDY	19			0,000	-1,000E-02	1,000E-02	L4:Right Surface: Y-Decenter, surface (mm)
104	TSTX	19			0,000	-4,000E-03	4,000E-03	L4:Right Surface: X-Tilt, surface (degree)
105	TSTY	19			0,000	-4,000E-03	4,000E-03	L4:Right Surface: Y-Tilt, surface (degree)
106	TOFF							L4:Right Surface End
107	TOFF							-----
108	TOFF							>>>Fifth Lens: L5
109	TOFF							L5:Left Surface
110	TTHI	21	21		10,173	-0,020	0,020	L5:Left Thickness (mm)
111	TRAD	21	0		130,657	-0,033	0,033	L5:Left Surface: Radius of Curvature (mm)

Figure C.4 Tolerance Data Editor for the final optical design-4.

112	TEDX	21	23		0,000	-0,020	0,020	L5:Left Surface: X-Decenter, element (mm)
113	TEDY	21	23		0,000	-0,020	0,020	L5:Left Surface: Y-Decenter, element (mm)
114	TETY	21	23		0,000	-0,015	0,015	L5:Left Surface: Y-Tilt, element (degree)
115	TETX	21	23		0,000	-0,015	0,015	L5:Left Surface: X-Tilt, element (degree)
116	TEZI	21	37	5	0,000	-7,900E-06	7,900E-06	L5:Left Surface: Zernike RMS WFE (mm)
117	TSDX	21			0,000	-1,000E-02	1,000E-02	L5:Left Surface: X-Decenter, surface (mm)
118	TSDY	21			0,000	-1,000E-02	1,000E-02	L5:Left Surface: Y-Decenter, surface (mm)
119	TSTX	21			0,000	-4,000E-03	4,000E-03	L5:Left Surface: X-Tilt, surface (degree)
120	TSTY	21			0,000	-4,000E-03	4,000E-03	L5:Left Surface: Y-Tilt, surface (degree)
121	TOFF							L5:Left Surface End
122	TOFF							L5:Right Surface
123	TTHI	23	23		118,375	-0,020	0,020	L5:Right Air Thickness (mm)
124	TRAD	23	0		-685,925	-0,171	0,171	L5:Right Surface: Radius of Curvature (mm)
125	TEZI	23	37	5	0,000	-7,900E-06	7,900E-06	L5:Right Surface: Zernike RMS WFE (mm)
126	TSDX	23			0,000	-1,000E-02	1,000E-02	L5:Right Surface: X-Decenter, surface (mm)
127	TSDY	23			0,000	-1,000E-02	1,000E-02	L5:Right Surface: Y-Decenter, surface (mm)
128	TSTX	23			0,000	-4,000E-03	4,000E-03	L5:Right Surface: X-Tilt, surface (degree)
129	TSTY	23			0,000	-4,000E-03	4,000E-03	L5:Right Surface: Y-Tilt, surface (degree)
130	TOFF							L5:Right Surface End
131	TOFF							Fifth Surface End !!!
132	TOFF							-----

Figure C.5 Tolerance Data Editor for the final optical design-5.

133	TOFF							>>>Sixth Lens: L6
134	TOFF							L6:Left Surface
135	TTHI	25	25		9,997	-0,020	0,020	L6:Left Thickness (mm)
136	TRAD	25	0		-88,244	-0,022	0,022	L6:Left Surface: Radius of Curvature (mm)
137	TEDX	25	27		0,000	-0,020	0,020	L6:Left Surface: X-Decenter, element (mm)
138	TEDY	25	27		0,000	-0,020	0,020	L6:Left Surface: Y-Decenter, element (mm)
139	TETY	25	27		0,000	-0,015	0,015	L6:Left Surface: Y-Tilt, element (degree)
140	TETX	25	27		0,000	-0,015	0,015	L6:Left Surface: X-Tilt, element (degree)
141	TEZI	25	37	5	0,000	-7,900E-06	7,900E-06	L6:Left Surface: Zernike RMS WFE (mm)
142	TSDX	25			0,000	-1,000E-02	1,000E-02	L6:Left Surface: X-Decenter, surface (mm)
143	TSDY	25			0,000	-1,000E-02	1,000E-02	L6:Left Surface: Y-Decenter, surface (mm)
144	TSTX	25			0,000	-4,000E-03	4,000E-03	L6:Left Surface: X-Tilt, surface (degree)
145	TSTY	25			0,000	-4,000E-03	4,000E-03	L6:Left Surface: Y-Tilt, surface (degree)
146	TOFF							L6:Left Surface End
147	TOFF							L6:Right Surface
148	TRAD	27	0		-226,881	-0,057	0,057	L6:Right Surface: Radius of Curvature (mm)
149	TEZI	27	37	5	0,000	-7,900E-06	7,900E-06	L6:Right Surface: Zernike RMS WFE (mm)
150	TSDX	27			0,000	-1,000E-02	1,000E-02	L6:Right Surface: X-Decenter, surface (mm)
151	TSDY	27			0,000	-1,000E-02	1,000E-02	L6:Right Surface: Y-Decenter, surface (mm)
152	TSTX	27			0,000	-4,000E-03	4,000E-03	L6:Right Surface: X-Tilt, surface (degree)
153	TSTY	27			0,000	-4,000E-03	4,000E-03	L6:Right Surface: Y-Tilt, surface (degree)
154	TOFF							L6:Right Surface End
155	TOFF							Sixth Surface End !!!
156	TOFF							-----

Figure C.6 Tolerance Data Editor for the final optical design-6.

CURRICULUM VITAE

BETÜL KONAKLI YAZGAN

Bahçelievler Mah. 06830 Gölbaşı, Ankara, Türkiye

EDUCATION

GAZİANTEP UNIVERSITY

Gaziantep, Turkey

MSc., Optical and Acoustic Engineer
2020 – 2024

BSc., Optical and Acoustic Engineer
2013 - 2018

EXPERIENCE

GAZIANTEP UNIVERSITY OPTICAL AND ACOUSTIC ENGINEERING DEPARTMENT

Gaziantep, Turkey

Optic laboratory volunteer assistant
Sept 2013 – Jun 2018

TÜBİTAK SPACE TECHNOLOGIES RESEARCH INSTITUTE

Ankara/Turkey

Research Intern
Feb – Jun 2018

TÜBİTAK SPACE TECHNOLOGIES AND RESEARCH INSTITUTE

Ankara, Turkey

Expert Researcher Engineer
January 2019 – Present

- Optical Alignment and Testing

    - Alignment of the Equipment Level
    - System-level Alignment (Laser Tracker)
    - Verification of Mechanical Assembly of Objectives (Vertical Autocollimator / Trioptics-OptiCentric)
    - Interferometric Optical Transfer Function (OTF) Measurement
    - Measurement of Optical Elements (Aspheric/Spherical Convex Mirror/ Concave Mirror / Flat Mirror) Surface Pro
- Optical Design
    - Determination of Optical System Requirements
    - Refractive Optical Design (SWIR, VIS)
    - Reflective Optical Design (Ritchey-Chretien)
    - Catadioptric Optical Design (Schmidt-Cassegrain, Maksutov-Cassegrain)
    - Analysis of the Optical Performance Impact of Optomechanical Structure
- Project Work on:
    - İMECE Imaging Satellite
    - TÜRKSAT 6A Communication Satellite
    - CubeSat

COMPUTER

- OpticStudio
- SolidWorks
- Dialux
- MATLAB
- Origin
- MS-Office
- Spatial Analyzer
- IMATEST

ACHIEVEMENTS

In 2018, Achieving first place in the Department of Optical And Acoustic Engineering at Gaziantep University.

2013-2014 Gaziantep University Optical and Acoustic Engineering, Cassegrain Telescope Project.

2016-2017 Gaziantep University Optical and Acoustic Engineering, Wireless Optical Communication (Undergraduate thesis).

2016-2017 Gaziantep University Optical and Acoustic Engineering Noise Measurement of Gaziantep University and Noise Mapping.

2016-2017 Gaziantep University Optical and Acoustic Engineering, Room Acoustic Calculation and Measurement with ODEON software.

2017-2018 Gaziantep University ARGETİ Project Market Championship Award (As part of the undergraduate thesis).

PUBLICATIONS

- B. K. Yazgan, M. Ekıncı, A. Bıngül and Ö. Karci, "Design of a Compact Telephoto Objective for 6U CubeSats," 2023 10th International Conference on Recent Advances in Air and Space Technologies (RAST), Istanbul, Turkiye, 2023, pp. 1-5, doi: 10.1109/RAST57548.2023.10197869.
- E. Arpa, B. K. Yazgan, M. Ekinci, Ö. Karcı, “Design of a Ritchey-Chretien (RC) Telescope with a Field Corrector for 12U Cubesats,” 2022 Ulusal Optik, Elektro-Optik ve FOTONİK Çalıştayı, Ankara,Türkiye, 2022.